TESI DI DOTTORATO

UNIVERSITÀ DEGLI STUDI DI NAPOLI "FEDERICO II"

DIPARTIMENTO DI INGEGNERIA BIOMEDICA,
ELETTRONICA E DELLE TELECOMUNICAZIONI

DOTTORATO DI RICERCA IN
INGEGNERIA ELETTRONICA E DELLE TELECOMUNICAZIONI

COMPRESSED SENSING: A NEW FRAMEWORK FOR SIGNALS RECOVERY AND ITS APPLICATION IN DIGITAL HOLOGRAPHY

PASQUALE MEMMOLO

Il Coordinatore del Corso di Dottorato	Il Tutore
Ch.mo Prof. Niccoló RINALDI	Ch.mo Prof. Antonia Maria TULINO

A. A. 2010–2011

"You will not really understand something until you are able to explain it to your grandmother!"

A. E.

"If you think I'm wrong, then you're wrong twice!"

P. M.

Acknowledgments

Firstly, I want to express my sincere gratitude to my family for their support and encouragement to pursue my dream of working in scientific research. Special thanks to Professor Antonia Tulino, my mentor and friend, who supported my research interests and aptitudes. Thanks to her, I could stay three months at Bell Laboratories in the U.S.A. where I could compare with excellent minds, learning a lot. Besides, I infinitely thank the National Institute of Optics of CNR, in particular Dr. Pietro Ferraro, who has followed me in many research activities in these three years of study, and Dr. Melania Paturzo, collaborator and dear friend, who shared with me "joys and sorrows" of my scientific activity and, obviously, the other colleagues Lisa, Sara, Veronica, Simonetta, Francesco and Andrea. Finally, I thank all the professors of DIBET, with particular regard to Professor Ernesto Conte, with who I have often been able to exchange views of both a scientific and everyday life.

Pasquale Memmolo

Contents

List of Figures

List of Tables

Introduction

Signal acquisition is a fundamental task of most contemporary digital systems. Due to the time varying nature of most practical signals, a great deal of adaptive and/or robust techniques as well as a fine tuning are required to get close to optimal reconstruction performances. A fundamental results in signal processing is the Nyquist/Shannon sampling theorem, which states that the number of samples needed to reconstruct a signal without error is determined by its bandwidth. This sampling procedure allows to transform any bandlimited continuous time signal in a discrete time signal without any loss of information, and at the same time, provides a direct way of reconstructing the original signal. However, there are two main problems which arise with this sampling technique. On one hand, sampling becomes more difficult when the frequency support of the signal spans through a larger bandwidth, on the other hand, depending on the entropy of the source, the discrete time signal produced by the sampling may contain redundant samples, making a source encoder necessary to describe the signal more compactly. Interestingly, the Nyquist/Shannon rate sampling theorem, which has dominated digital processing in science and technology since its origins, can be surprisingly leaped over through Compressed Sensing (CS) theory. In fact, because most signals of practical interest admit a sparse representation in a given basis, the emergent framework of Compressed Sensing (CS) [1],[2], can potentially provide a practical solution. It exploits the underlying sparsity, like l_0 and l_1 minimization techniques as well as all suitable greedy algorithms typical of the CS literature. Recently, it has shown that [1],[2],[3],[4],[5],[6] a signal having a sparse representation can be recovered exactly from a small set of linear, non-adaptive measurements. This result suggests that it may be possible to sense sparse signals by taking far fewer measurements, hence the name *compressed* sensing. However, there are three principal differences between the classical sampling and the CS. Firstly, sampling theory typically considers infinite length, continuous-time signals, while CS is a mathematical theory focused on

measuring finite-dimensional vectors in R^n. Secondly, rather than sampling the signal at specific points in time, CS systems typically acquire measurements in the form of inner products between the signal and more general test functions. Thirdly, the two frameworks differ in the manner in which they deal with signal recovery, i.e., the problem of recovering the original signal from the compressive measurements. In the Nyquist-Shannon framework, signal recovery is achieved through sinc-function interpolation, while, in CS, signal recovery is typically achieved using highly nonlinear methods [7].

In recent years, CS has attracted considerable attention in areas of applied mathematics, computer science, and electrical engineering by suggesting that it may be possible to surpass the traditional limits of sampling theory. CS builds upon the fundamental fact that we can represent many signals using only a few non-zero coefficients in a suitable basis, i.e. sparse representation in a particular domain. Sparsity has long been exploited in signal processing and approximation theory for tasks such as compression [8] and denoising [9], and in statistics and learning theory as a method for avoiding overfitting [10]. Sparsity also figures prominently in the theory of statistical estimation and model selection [11], in the study of the human visual system [12], and has been exploited heavily in image processing tasks, since the multiscale wavelet transform [13] provides nearly sparse representations for natural images. The recent results in [14] have proved insight on the theoretical bounds for the support recovery error rate of the sparse signal, and at the same time has established a link between compressed sensing, information theory, statistical physics and random matrix theory. However, the interdisciplinary nature of CS, as connected to information theory, signal processing, communications, algorithm design (such as belief propagation), statistical physics and other related fields, has not been yet fully explored. In particular, in this thesis we present the application of CS framework in the field of Digital Holography (DH) [15],[16],[17], that is a relatively recent interferometric technique. Holographic basic principle is the recording of an interference pattern on a photographic plate (classical holography) or by a charge coupled device (digital holography). In the latter case, from the reconstructed wavefront, it is possible to manage the amplitude as well as the phase of the optical wavefield. The capability to perform amplitude image and phase contrast image makes DH a suitable tool in many application fields from metrology to 3D display. Some of the applications of CS in DH are described in [18],[19] for improvements in terms of experimental schemes, compression and recently for holograms denoising [20]. Therefore, the thesis is focused on the aforementioned tasks in DH with a particular attention on the

problem of the denoising in DH for an efficient reconstruction and 3D display.

In the first part of this thesis, the CS theory is described mathematically as well as the holographic process, then the second part considers the principal results of the application of CS in DH. More precisely, Chapter 1 includes the mathematical formulation of CS theory, focused firstly on the property of sparsity for the signals, then on the design of a sensing matrices that can be used to recover the signals from undersampled measurements, and finally on the noiseless as well as noisy signal recovery. In addition there is a description of the most popular recovery algorithms that can be applied for both noiseless and noisy signals. Chapter 2 contains the theoretical description of the full holographic process (optical and digital), from the recording to the reconstruction, considering digital holograms recorded in both microscope and lensless configurations. Using the discrete version of the Fresnel integral, the analysis of the diffracted complex field is achieved through the in-focus numerical reconstructions for both kind of digital holograms and the BFP reconstructions for the digital holograms recorded in microscope configuration. It is shown also the phase reconstructions and is proposed an algorithm of automatic search of the in-focus reconstruction distance and BFP distance. Chapter 3 addresses the combination between CS and DH in order to achieve a general imaging scheme to optimize the digital recording. In particular, through the application of the CS, we are able to recover the digital holograms using undersampled measurements. It is also proposed an unified procedure of recovery of both classes of aforementioned digital holograms, based on the sparsity transform that is suitable for the different types of digital holograms, i.e. microscope recording and lensless recording. Several examples are considered to confirm the choice of the transform domain. In the Chapter 4 we address to the problem of recovery of the noisy digital holograms and we propose a new greedy algorithm, based on a simple modification of the sparsity minimization algorithm, that permits to achieve an efficient and robust denoising without any prior information about the statistics of noise. Also in this case, several example are considered to test the proposed method, which is compared with other two denoising algorithms. In addition, display tests are performed in order to show the effectiveness of the new denoising algorithm. Finally, upon completion of the dissertation, there are two appendices. the first one is focused on a simple review of the Convex Optimization theory, on which the recovery algorithms are based, while in the second one there is a description of the MATLAB scripts realized to implement the algorithms for DH analysis and recovery.

Chapter 1

Compressed Sensing

The sampling of continuous-time band limited signals is the theoretical basis on which it has developed the digital revolution. The works of Nyquist [21] and Shannon [22] show that the signals can be exactly recovered from a set of uniformly spaced samples, taken at the Nyquist rate of twice the highest frequency present in the signal of interest and, capitalizing on this discovery, much of signal processing has moved from the analog to the digital domain. Unfortunately, in many important applications, the resulting Nyquist rate is so high that we end up with far too many samples. Therefore, despite extraordinary advances in computational power, the acquisition and processing of signals in several application areas continues to pose a remarkable challenge. Using the same concept of transform coding [23],[24], Compressed Sensing (CS) has emerged as a new framework for signal acquisition. CS enables a potentially large reduction in the sampling and computation costs for sensing signals that have a sparse or compressible representation. While the Nyquist/Shannon sampling theorem states that a certain minimum number of samples is required in order to perfectly capture an arbitrary bandlimited signal, when the signal is sparse in a known basis we can reduce the number of measurements that need to be stored. Consequently, when sensing sparse signals we might be able to do better than suggested by classical results. The works of Candés, Romberg, Tao and Danoho [1-6] demonstrate that a finite-dimensional signal having a sparse or compressible representation can be recovered from a small set of linear, nonadaptive measurements. In other word, they claim that it may be possible to sense sparse signals by taking far fewer measurements. In this chapter, there is a mathematical description of CS. The first section is focused on the property of sparsity for the signals, then the de-

sign of a sensing matrices for different applications and finally the description of the problem of signal recovery in both cases of noiseless and noisy signals. Finally, there is a description of the most popular algorithms able to solve the recovery problem.

1.1 Sparse signals

Signals can often be well-approximated as a linear combination of just a few elements from a known basis or dictionary. When this representation is exact we say that the signal is sparse. Sparse signal models provide a mathematical framework for capturing the fact that in many cases these high-dimensional signals contain relatively little information compared to their ambient dimension. Mathematically, we say that a signal $\mathbf{x}$, represented by a n-vector, is k-sparse when it has at most k nonzeros

$$\Sigma_k = \{\mathbf{x} : \|\mathbf{x}\|_0 \leq k\} \tag{1.1}$$

where $\|\cdot\|_0$ is the l_0-norm. Σ_k denote the set of all k-sparse signals. Typically, we will be dealing with signals that are not themselves sparse, but which admit a sparse representation in some basis $\mathbf{\Psi}$, that is an $n \times n$ matrix, and, in this case we will still refer to $\mathbf{x}$ as being k-sparse, with the understanding that we can express $\mathbf{x}$ as $\mathbf{x} = \mathbf{\Psi c}$ with $\|\mathbf{c}\|_0 \leq k$. The vector $\mathbf{c}$ represent the set of n coefficients obtained by the projections of the signal on the basis and they can be computed as $c_i = \langle \mathbf{x}, \psi_i \rangle$, $i = 1, \ldots, n$, where $\{\psi_i\}_{i=1}^n$ are the vectors of orthonormal basis.

As a traditional application of sparse models, we consider the problems of image compression and image denoising. Most natural images are characterized by large smooth or textured regions and relatively few sharp edges. Signals with this structure are known to be very nearly sparse when represented using a multiscale wavelet transform [13]. In a wavelet transform of a typical natural image, most coefficients are very small. Hence, a good approximation of the signal can be obtain by setting the small coefficients to zero to obtain a k-sparse representation.

1.1.1 Geometry of sparse signals

Sparsity is a highly nonlinear model, since the choice of which dictionary elements are used can change from signal to signal [25]. This can be seen by observing that, given a pair of k-sparse signals, a linear combination of the

two signals will in general no longer be k sparse, since their supports may not coincide. That is, for any $\mathbf{x}, \mathbf{z} \in \Sigma_k$ we do not necessarily have that $\mathbf{x}+\mathbf{z} \in \Sigma_k$. The set of sparse signals Σ_k does not form a linear space. Instead, it consists of the union of all possible $\begin{pmatrix} n \\ k \end{pmatrix}$ canonical subspaces. For larger values of n and k we must consider a potentially huge number of subspaces. This will have significant algorithmic consequences in the development of the algorithms for sparse approximation and sparse recovery.

1.1.2 Compressible signals

An important point in practice is that few real-world signals are *truly* sparse. Rather they are compressible, meaning that they can be well-approximated by a sparse signal. Such signals have been termed compressible, approximately sparse, or relatively sparse in various contexts. Compressible signals are well approximated by sparse signals in the same way that signals living close to a subspace are well approximated by the first few principal components [26]. In fact, we can quantify the compressibility by calculating the error incurred in the approximation of a signal $\mathbf{x}$ by some $\hat{\mathbf{x}} \in \Sigma_k$

$$\sigma_{k,p}(\mathbf{x}) = \min_{\hat{\mathbf{x}} \in \Sigma_k} \|\mathbf{x} - \hat{\mathbf{x}}\|_p \tag{1.2}$$

where $\|\cdot\|_p$ is the l_p-norm. If $\mathbf{x} \in \Sigma_k$ then obviously $\sigma_{k,p}(\mathbf{x}) = 0 \; \forall p$.

1.2 Sensing matrices

In this section there is the description of the standard finite-dimensional CS model. Given a signal $\mathbf{x} \in R^n$ and a measurement systems that acquire m linear measurements, we can represent this process mathematically as

$$\mathbf{y} = \mathbf{\Phi}\mathbf{x} \tag{1.3}$$

where $\mathbf{\Phi}$ is an $m \times n$-matrix and $\mathbf{y}$ is a m-vector. The matrix $\mathbf{\Phi}$ represents a dimensionality reduction, i.e., it maps R^n into R^m where typically $m \ll n$. Note that in the standard CS framework we assume that the measurements are non-adaptive, meaning that the rows of $\mathbf{\Phi}$ are fixed in advance and do not depend on the previously acquired measurements. In certain settings, adaptive measurement schemes can lead to significant performance gains. As noted earlier, although the standard CS framework assumes that $\mathbf{x}$ is a finite-length vector

with a discrete-valued index (such as time or space), in practice we will often be interested in designing measurement systems for acquiring continuously-indexed signals such as continuous-time signals or images. It is sometimes possible to extend this model to continuously-indexed signals using an intermediate discrete representation. For now, we will simply think of x as a finite-length window of Nyquist-rate samples, and we will temporarily ignore the issue of how to directly acquire compressive measurements without firstly sampling at the Nyquist rate. In the following subsection, we give details about how to design the sensing matrix $\mathbf{\Phi}$ to ensure that it preserves the information in the signal $\mathbf{x}$ and how can be recovered the original signal $\mathbf{x}$ from the measurements $\mathbf{y}$. Because we want consider the case in which our data is sparse or compressible, we will see that we can design matrices $\mathbf{\Phi}$ with $m \ll n$ that ensure that we will be able to recover the original signal accurately and efficiently using a variety of practical algorithms. In the following we consider firstly a few desirable properties that we might wish $\mathbf{\Phi}$ to have and finally we give a design procedure.

1.2.1 Null space condition

A natural place to begin is by considering the null space of $\mathbf{\Phi}$, denoted

$$\mathcal{N}(\mathbf{\Phi}) = \{\mathbf{z} : \mathbf{\Phi z} = 0\} \tag{1.4}$$

If we wish to be able to recover all sparse signals $\mathbf{x}$ from the measurements $\mathbf{\Phi x}$, then it is immediately clear that for any pair of distinct vectors $\mathbf{x}, \mathbf{x}' \in \Sigma_k$, we must have $\mathbf{\Phi x} \neq \mathbf{\Phi x}'$, otherwise it would be impossible to distinguish $\mathbf{x}$ from $\mathbf{x}'$ based solely on the measurements $\mathbf{y}$. This concept is expressed by the following theorem

Theorem 1.1: $\mathbf{\Phi}$ *uniquely represents all* $\mathbf{x} \in \Sigma_{\mathrm{k}}$ *if and only if* $\mathcal{N}(\mathbf{\Phi})$ *contain no vector in* $\Sigma_{2\mathrm{k}}$.
Proof: *if* $\mathbf{\Phi x} = \mathbf{\Phi x}'$, *then* $\mathbf{\Phi}(\mathbf{x} - \mathbf{x}') = 0$ *with* $\mathbf{x} - \mathbf{x}' \in \Sigma_{2\mathrm{k}}$.

1.2.2 The restricted isometry property

When the measurements are contaminated with noise or have been corrupted by some errors such as quantization, it will be useful to consider somewhat stronger conditions. In [27], Candés and Tao introduced the following isometry condition on matrices $\mathbf{\Phi}$ and established its important role in CS.

Definition 1.1: *The matrix $\mathbf{\Phi}$ satisfies the restricted isometry property (RIP) of order k if there exists a $\delta_k \in (0,1)$ such that*

$$(1-\delta_k)\|\mathbf{x}\|_2^2 \leq \|\mathbf{\Phi x}\|_2^2 \leq (1+\delta_k)\|\mathbf{x}\|_2^2 \tag{1.5}$$

holds $\forall \mathbf{x} \in \Sigma_{\mathrm{k}}$

If a matrix $\mathbf{\Phi}$ satisfies the RIP, then this is sufficient for a variety of algorithms to be able to successfully recover a sparse signal from noisy measurements.

1.2.3 Coherence matrices

While the Null Space Condition (NSP) and RIP all provide guarantees for the recovery of k-sparse signals, verifying that a general matrix $\mathbf{\Phi}$ satisfies any of these properties has a combinatorial computational complexity, since in each case one must essentially consider $\begin{pmatrix} n \\ k \end{pmatrix}$ submatrices. In many cases it is preferable to use properties of $\mathbf{\Phi}$ that are easily computable to provide more concrete recovery guarantees. The coherence of a matrix is one such property [28],[29].

Definition 1.2: *The coherence of a matrix $\mathbf{\Phi}$ is the largest absolute inner product between any two columns ϕ_i, ϕ_j of (Φ)*

$$\mu(\mathbf{\Phi}) = \max_{1 \leq i < j \leq n} \frac{|\langle \phi_i, \phi_j \rangle|}{\|\phi_i\|_2 \|\phi_j\|_2} \tag{1.6}$$

It is possible to show that the coherence of a matrix is always in the range $\mu(\mathbf{\Phi}) \in \left[\sqrt{\frac{m-n}{m(n-1)}}, 1\right]$, where the lower bound is known as the Welch bound [30],[31].

1.2.4 Sensing matrix construction

The goal of this section is to show the different choice of sensing matrix that satisfied the three conditions defined above, i.e NSP, RIP and Coherence. Despite there are well known matrices that verified the above properties as for example the Vandermonde matrix [32], the Gabor frame generated from the Alltop sequence [33] and more general equiangular tight frames [31] and others. Unfortunately, in many real-world settings, these results would lead to an unacceptably large requirement on m dimension. These limitations can

be overcome by randomizing the matrix construction. For example, it can be shown that random matrices will satisfy the RIP with high probability if the entries are chosen according to a Gaussian, Bernoulli, or more generally any sub-gaussian distribution. In addition, using random matrices to construct $\mathbf{\Phi}$ has a different benefits. It is possible to recover a signal using any sufficiently large subset of the measurements [34]. More important is that, in practice, we are often more interested in the setting where $\mathbf{x}$ is sparse with respect to some basis $\mathbf{\Psi}$. In this case what we actually require is that the product $\mathbf{\Phi\Psi}$ satisfies the RIP. If we were to use a deterministic construction then we would need to explicitly take $\mathbf{\Psi}$ into account in our construction of $\mathbf{\Phi}$, but when $\mathbf{\Phi}$ is chosen randomly we can avoid this consideration.

Therefore, to recover efficiently the signal $\mathbf{x}$, the much simple choice is to take $\mathbf{\Phi}$ according to any sub-gaussian distributions and $\mathbf{\Psi}$ as an orthonormal basis. In fact, in this case it can easily show that the matrix $\mathbf{\Phi\Psi}$ will also have a sub-gaussian distribution, and so provided that m is sufficiently high $\mathbf{\Phi\Psi}$ will satisfy the RIP with high probability. This property, sometimes referred to as *universality*, constitutes a significant advantage of using random matrices to construct $\mathbf{\Phi}$.

1.3 Signal recovery via l_1-minimization

Now we consider a natural first approach to the problem of sparse recovery. Given measurements $\mathbf{y}$ and the knowledge that our original signal $\mathbf{x}$ is sparse (or compressible) in a particular basis $\mathbf{\Psi}$, it is natural to attempt to recover $\mathbf{x}$ by solving the following optimization problem

$$\widehat{\mathbf{x}} = \arg\min \ \|\mathbf{\Psi x}\|_0 \quad \text{subject to} \quad \mathbf{x} \in S(\mathbf{y}) \tag{1.7}$$

where the set $S(\mathbf{y})$ ensures that $\widehat{\mathbf{x}}$ is consistent with the measurements. The objective function in (1.7) is nonconvex, therefore the research of a solution that approximates the true minimum is an NP-hard problem. However, by minimizing the ℓ_1-norm instead, the relaxation leads to the convex problem

$$\widehat{\mathbf{x}} = \arg\min \ \|\mathbf{\Psi x}\|_1 \quad \text{subject to} \quad \mathbf{x} \in S(\mathbf{y}) \tag{1.8}$$

which makes it computationally feasible if $S(\mathbf{y})$ is convex. The relaxation is justified to the fact that, within the CS framework, it is well known that in the absence of additive Gaussian noise, l_0 and l_1-minimization techniques allow perfect reconstruction of the original sparse signal. This property, in

conjunction with the Lipschitz continuity of the l_0 and l_1 norms, guarantees, in the presence of low-power noise, a robust performance in terms of signal reconstruction. In the hypothesis that the constraint $S(\mathbf{y})$ is convex, it can be formulated the optimization problem (1.8) as a linear programming problem, that is typically considered computationally tractable. More details about the relaxation procedure and linear programming is give in Appendix A.1. Now we consider two different formulation of the optimization problem (1.8) related to the choice of the constraint.

1.3.1 Noiseless signal recovery

In the case in which the measurements $(\mathbf{y})$ are exact and noise-free, we can take the set $S(\mathbf{y})$ as

$$S(\mathbf{y}) = \{\mathbf{x} : \mathbf{y} = \mathbf{\Phi\Psi x}\} \tag{1.9}$$

and the optimization problem (1.8) becomes

$$\widehat{\mathbf{x}} = \arg\min \ \|\mathbf{\Psi x}\|_1 \quad \text{subject to} \quad \mathbf{y} = \mathbf{\Phi\Psi x} \tag{1.10}$$

In literature several algorithms that permit to solve the problem (1.10) in an efficient computational time exist. In fact, this problem has been studied in the signal analysis literature under the name Basis Pursuit (BP) [35]. Other recent algorithms are Orthogonal Matching Pursuit (OMP) [36] and Stagewise Orthogonal Matching Pursuit (StOMP) [37], which is a greedy algorithm similar to OMP, but faster than it, in the sense that it requires less iterations in the recovery process. The description of these algorithm is reported in the section 1.4.

1.3.2 Noisy signal recovery

The ability to perfectly reconstruct a sparse signal from noise-free measurements represents a very promising result. However, in most real-world systems the measurements are likely to be contaminated by some form of noise. In fact, systems which are implemented in physical hardware will be subject to a variety of different types of noise depending on the setting. Another important noise source is on the signal itself. In many settings the signal $\mathbf{x}$ to be estimated is contaminated by some form of random noise. The implications of this type of noise on the achievable sampling rates has been recently analyzed in [38],[39],[40]. Therefore, it is very important to consider a much real case

of recovering in which we have a noisy signals. In this case, we can take the set $S(\mathbf{y})$ as

$$S(\mathbf{y}) = \{\mathbf{x} : \|\mathbf{y} - \Phi\Psi\mathbf{x}\|_{\mathbf{2}} \leq \epsilon\} \tag{1.11}$$

where ϵ is a system parameter dependent on the noise variance. Replacing this constraint in the problem (1.8), it becomes

$$\widehat{\mathbf{x}} = \arg\min \ \|\mathbf{\Psi x}\|_1 \quad \text{subject to} \quad \|\mathbf{y} - \Phi\Psi\mathbf{x}\|_2 \leq \epsilon \tag{1.12}$$

To solve this problem, typically it uses the Least Angle Regression (LARS) algorithm [41] of which there is a brief description in the following section.

1.4 Algorithms for signal recovery

In this appendix there is a description of different algorithms able to solve the convex optimization problem (1.10). First of all, it is shown how to reformulate this problem as a LP. In fact, write it out in an equivalent form, with $\theta = \mathbf{\Psi x}$ being the optimization variable:

$$\min \ \|\theta\|_1 \quad \text{subject to} \ \ \mathbf{y} = \mathbf{\Phi}\theta \tag{1.13}$$

This can be formulated as a linear programming problem: let $A = [\mathbf{\Phi} \ \ -\mathbf{\Phi}]$ be the $m \times 2n$ matrix. The following LP

$$\min \ \mathbf{1}^T\mathbf{z} \ \text{ subject to } \ \mathbf{y} = \mathbf{A}\mathbf{z}, \qquad \mathbf{z} \succeq 0 \tag{1.14}$$

has an optimal solution $\mathbf{z}^* \in R^{2n}$ which can be partitioned as $\mathbf{z}^* = [\mathbf{u}^* \ \ \mathbf{v}^*]$ with $\mathbf{u}^*, \mathbf{v}^* \in R^n$. It is possible to show that [2] the optimal solution of problem (1.13) is $\theta^* = \mathbf{u}^* - \mathbf{v}^*$ and, therefore, $\mathbf{x}^* = \mathbf{\Psi}^T\theta^*$ is the optimal solution of the problem (1.10). Similar calculations lead to the optimal solution also for the optimization problem (1.12)

1.4.1 Basis Pursuit

BP [35] finds signal representations in overcomplete dictionaries by convex optimization. It obtains the decomposition that minimizes the l_1 norm of the coefficients occurring in the representation. Because of the non differentiability of the l_1 norm, this optimization principle leads to decompositions that can have very different properties from the Method of Frames [42]. Because it is

based on global optimization, it can stably super-resolve in ways that Matching Pursuit (MP) [43] can not. BP can be used with noisy data by solving an optimization problem trading off a quadratic misfit measure with an l_1 norm of coefficients. It can stably suppress noise while preserving structure that is well-expressed in the dictionary under consideration. The principle of BP is to find a representation of the signal that solves the optimization problem (1.13). The BP problem can be reformulated as a LP in the standard form by making the translations given in Eq. (1.14). Several algorithms from the LP literature as a candidate for solving the BP optimization problem. Both the simplex and interior-point algorithms offer interesting insights into BP.

With a simple changes, the optimization problem (1.13) becomes a denoising problem. It is called Basis Pursuit De-Noising [35] (BPDN), and refers to solution of

$$\min \ \frac{1}{2} \|\mathbf{y} - \mathbf{\Phi}\theta\|_2^2 + \epsilon \|\theta\|_1 \tag{1.15}$$

where the solution $\hat{\theta}$ is a function of the parameter ϵ, that controls the size of the residual. In [44] is showed that this optimization problem can be solved using the perturbed linear programming, that is a quadratic programming, but retains structure similar to LP.

1.4.2 Orthogonal Matching Pursuit

A family of iterative greedy algorithms are shown to have the approximate reconstruction property, generally with small computational complexity. Such algorithms include MP [43], OMP [29],[36] and their derivations [45],[46]. OMP iteratively incorporates in the reconstructed signal the component from the measurement set that explains the largest portion of the residual from the previous iteration [29]. With reference to the optimization problem (1.13) the algorithm is

Algorithm 1 (OMP)
INPUT:

- Sensing matrix $\mathbf{\Phi} \in R^{m \times n}$
- Vector of measurement $\mathbf{y} \in R^m$

OUTPUT:

- Signal estimated $\hat{\theta} \in R^n$

- Support estimated Λ_K, where K is the number of iterations
- Residual $\mathbf{r}^{(K)} \in R^m$

PSEUDOCODE

- Initialization: $\mathbf{r}^{(0)} = y$, $\Lambda^{(0)} = \emptyset$
- Repeat until $\{$stopping criteria$\}$
  $c_i^{(k)} = \langle \phi_i \mathbf{r}^{(k-1)} \rangle$
  $\lambda^{(k)} = \arg\max_i |c_i^{(k)}|$
  $\Lambda^{(k)} = \Lambda^{(k-1)} \cup \{\lambda^{(k)}\}$
  $\mathbf{\Phi}^{(k)} = [\mathbf{\Phi}^{(k)} \phi_{\lambda^{(k)}}]$
  $\theta^{(k)} = \arg\min_\theta \|\mathbf{y} - \mathbf{\Phi}^{(k)}\theta\|_2^2$
  $\mathbf{r}^{(k)} = \mathbf{y} - \mathbf{\Phi}^{(k)}\theta^{(k)}$

The stopping criteria can be a fixed number of iterations or iterate until $\|\mathbf{r}^{(k)}\|_2 \leq \varrho$, with a predeterminate $\varrho \geq 0$. The conditions for proper termination involve knowledge of the signal sparsity or the noise variance to achieve the desired denoising effect.

1.4.3 Stagewise Orthogonal Matching Pursuit

StOMP [37] aims to achieve an approximate solution to $\mathbf{y} = \mathbf{\Phi}\theta$, where the sensing matrix $\mathbf{\Phi}$ comes from the Uniform Spherical ensemble (USE). It operates in S iterations, building up a sequence of approximations $\theta^{(0)}, \ldots \theta^{(S)}$ by removing detected structure from a sequence of residual vectors $\mathbf{r}^{(0)}, \ldots \mathbf{r}^{(S)}$. For each $s = 1, \ldots, S$, let $I^{(s)}$ the estimation of the locations of the nonzeros in $\theta^{(s)}$, $\sigma^{(s)}$ a formal noise level, $t^{(s)}$ a threshold parameter, $\mathbf{\Phi}_{I^{(s)}}$ the $m \times |I^{(s)}|$ matrix with columns chosen using index set $I^{(s)}$, the algorithm operates as follow

Algorithm 2 (StOMP)
INPUT:

- Sensing matrix $\mathbf{\Phi} \in R^{m \times n}$
- Vector of measurement $\mathbf{y} \in R^m$

OUTPUT:

- Sequence of signal estimated $\theta^{(0)}, \ldots \theta^{(S)}$

- Sequence of the residual $\mathbf{r}^{(0)}, \ldots \mathbf{r}^{(S)}$
- Sequence of estimates $I^{(1)}, \ldots, I^{(S)}$ of the locations of the nonzeros

PSEUDOCODE

- Initialization: $\mathbf{r}^{(0)} = y$, $\theta^{(0)} = 0$
- Repeat until $\{s \leq S\}$
  $\mathbf{c}^{(s)} = \mathbf{\Phi}^T \mathbf{r}^{(s-1)}$
  $J^{(s)} = \{j : |\mathbf{c}_j^{(s)}| \geq t^{(s)} \sigma^{(s)}\}$
  $I^{(s)} = I^{(s-1)} \cup J^{(s)}$
  $\left(\theta^{(s)}\right)_{I^{(s)}} = \left(\mathbf{\Phi}_{I^{(s)}}^T \mathbf{\Phi}_{I^{(s)}}\right)^{-1} \mathbf{\Phi}_{I^{(s)}}^T \mathbf{y}$
  $\mathbf{r}^{(s)} = \mathbf{y} - \mathbf{\Phi}^{(s)} \theta^{(s)}$
  $s := s + 1$

The term $\left(\theta^{(s)}\right)_{I^{(s)}}$ represents the approximation $\theta^{(s)}$ supported in $I^{(s)}$. StOMP runs much faster than competing proposals for sparse solutions, such as l_1 minimization and OMP, and so is attractive for solving large-scale problems.

1.4.4 Least Angle Regression method

LARS [41] is a new model selection algorithm that is a useful and less greedy version of traditional forward selection methods. Both Lasso and Stagewise are variants of a basic procedure called of Least Angle Regression, abbreviated LARS (the final *S* suggesting *Lasso* and *Stagewise*). LARS is a stylized version of the Stagewise procedure that uses a simple mathematical formula to accelerate the computations. The steps of the LARS algorithm are listed below

- Start with all coefficients equal to zero.
- At iteration $\beta = 1$, find the predictor most correlated with the response, say p_1.
- At iteration $\beta = 2$ take the largest step possible in the direction of this predictor until some other predictor, say p_2, has as much correlation with the current residual.
- At iteration $\beta = 3$, proceed in a direction equiangular between the two predictors until a third variable p_3

- Repeat until $\beta = B$

Therefore, the LARS algorithm proceeds equiangularly between $\beta - 1$ predictors, i.e. along the *least angle direction*, until a βth variable enters, for $\beta = 1, \ldots, B$.

Chapter 2

Digital Holography

Holography got its name from the Greek words *holos*, meaning whole, and *graphein*, meaning to write. It is a means for recording and reconstructing the whole information contained in an optical wavefront, namely amplitude and phase, and not just intensity as in photography. Dennis Gabor invented holography in 1948 as a lensless process for image formation by reconstructed wavefront with the aim of improving electron microscope images [47]. Gabor's ideas was unsuccessful in the field of electron microscopy because of practical problems but its validity in the optical field was confirmed by other researches [48], [49]. Because of the superimposition and the poor quality of the reconstructed images, the interest around holography declined up to the 1960s when the development of lasers made available a powerful source of coherent light. Holography is made of two separated processes: the recording of the hologram, and the object retrieval. The first stage is accomplished by means of a photographic film recording the interference pattern produced by the light waves scattered by an object and a reference beam derived from the same coherent light source, as shown in Figure 2.1 (a). Since the intensity at any point in this interference pattern also depends on the phase of the object wave, the resulting recording (the hologram) contains information on the phase as well as the amplitude of the object wave. The second stage is the formation of the object's image. If the hologram is illuminated once again with the original reference wave, as shown in Figure 2.1 (b), it reconstructs the original object wave. Indeed, when the hologram was illuminated with the original collimated beam, it produced two diffracted waves, one reconstructing an image of the object in its original location, and the other, with the same amplitude but the opposite phase, forming a second, conjugate image. A ma-

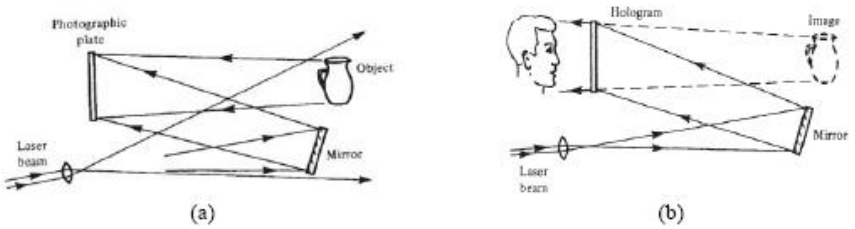

Figure 2.1: (a) Hologram recording: the interference pattern produced by the reference wave and the object wave is recorded; (b) Image reconstruction: light diffracted by the hologram reconstructs the object wave.

jor drawback of the technique proposed in [47] was the poor quality of the reconstructed image, because it was degraded by the conjugate image, which was superimposed on it, as well as by scattered light from the directly transmitted beam. The twin-image problem was solved in [50], [51] by developing of the off-axis reference beam technique. They used a separate reference wave incident on the photographic plate at an appreciable angle in respect to the object wave. As a result, when the hologram was illuminated with the original reference beam, the two images were separated by large enough angles from the directly transmitted beam, and from each other, to ensure that they did not overlap. Holography became a working tool to record and reconstruct whole wavefields both in amplitude and phase and thanks to this unique feature it found application in numerous fields. One of the most important is the use od holographic interferometry in the field of interferometric metrology [52], [53]. This technique allows the measurement of the changes of the phase of the wavefield and thus the changes of any physical quantities that affect the phase. The idea of using computer for reconstructing a hologram was first proposed by Goodman and Laurence in 1967 and then by Kronrod et al. [15], [54]. However, numerical reconstruction of imaged objects has been accomplished quite recently [17]. The development of computer technology and solid state image sensors made it possible to record hologram directly on charge coupled device (CCD) cameras. This important step enabled full digital recording and reconstruction of holograms without the use of photographic media, commonly referred to as digital holography (DH). Since then, many spectacular applications have been demonstrated such as microscopic imaging by phase-contrast digital holographic microscopy [55], 3D object recognition [56] and

3D dynamic display [57]. This chapter describes the entire holographic process by a detailed analysis of image formation in digital Fresnel holography [58].

2.1 Hologram formation

Phenomena involved in a digital holographic process are linear processes. Thus, it seems to be a pertinent way to search for a general relation between object and image that includes convolution products. The main processes that must be taken into account are the following: diffraction, interferences, spatial integration and sampling by pixels, and digital reconstruction. The reconstructed field can be written in the form of a convolution product between the real object and the impulse response of the full digital holographic process. Considering a reference system of coordinates $\{x, y\}$, attached to the principal surface of a real object, and a z-axis, perpendicular to this surface, that corresponds to the propagation direction of the diffracted light beam, we have

$$F_R(x, y) = F(x, y) \otimes T(x, y) \tag{2.1}$$

where $F_R(x, y)$ is the reconstructed field, $F(x, y)$ is the real object and $T(x, y)$ is the full process related to the image formation. The object surface illuminated by a coherent beam produces the following object wavefront

$$F(x, y) = F_0(x, y) \exp\left(j\phi_0(x, y)\right) \tag{2.2}$$

where $\phi_0(x, y)$ is related to the roughness of the object surface and can be modeled as uniformly distributed, i.e. $\phi_0(x, y) \sim \mathrm{U}(-\pi, \pi)$. Is possible that the object is not perfectly centered in the reference set of coordinates x,y but it is slightly laterally shifted at coordinate $\{x_0, y_0\}$. Without loss of generality, we consider the case $x_0 = y_0 = 0$.

The object wavefront propagates through at distance d_0, in which the reference set of coordinates is chosen to be $\{x', y'\}$, and the diffracted field produced by the object is given in the Fresnel approximations [59] by

$$\begin{aligned} O(x', y', d_0) &= \frac{j \exp\left[j\frac{2\pi d_0}{\lambda}\right]}{\lambda d_0} \int\int_{R^2} F(x, y) \times \\ &\times \exp\left\{j\frac{\pi}{\lambda d_0}\left[(x - x')^2 + (y - y')^2\right]\right\} dxdy \end{aligned} \tag{2.3}$$

where λ is the wavelength of beam. The distance d_0 is called recording distance. With a simple mathematical manipulation, we can rewrite Eq. (2.3)

in terms of Fourier Transform ($\mathcal{FT}$)

$$O(x', y', d_0) = Z(x', y', d_0)\mathcal{FT}\left\{F(x, y)W(x, y, d_0)\right\} \tag{2.4}$$

with

$$\begin{cases} Z(x', y', d_0) = \frac{j}{\lambda d_0} \exp\left\{\frac{2\pi}{\lambda}\left[d_0 + \frac{x'^2+y'^2}{2d_0}\right]\right\} \\ W(x, y, d_0) = \exp\left\{j\frac{\pi}{\lambda d_0}\left(x^2 + y^2\right)\right\} \end{cases} \tag{2.5}$$

As shown in Eq. (2.4), each optical field consists of an amplitude distribution as well as a phase distribution but all detectors or recording material only register intensity: the phase is lost in registration process. If two waves of the same frequency interfere, the resulting intensity distribution is temporally stable and depends on the phase difference. This is used in holography where the phase information is coded by interference into a recordable intensity. The diffracted field produced in Eq. (2.4) interferes with a reference wave having spatial coordinates $\{u_R, v_R\}$ on the plane $\{x', y'\}$

$$R(x', y') = a_R \exp\left\{j2\pi\left(u_R x' + v_R y'\right) + j\Omega\left(x', y'\right)\right\} \tag{2.6}$$

where the terms $\Omega\left(x', y'\right)$ corresponds to aberrations of the reference wavefront. The choice for a plane reference wave is motivated by the fact that, if the reference wave is spherical, its curvature can be inserted in the computation of the diffracted field [60], but if the curvature is false, this results in a focusing error. Furthermore, in off-axis Fresnel holography, the main parameter is the spatial frequencies of the reference wave, even if it is plane or spherical. This parameter is related to the angle between the object diffracted wave and the reference wave (see figure).

Finally, in the interference plane, the hologram H is written as

$$\begin{array}{rcl} H(x', y', d_0) & = & \left|O(x', y', d_0)\right|^2 + \left|R(x', y')\right|^2 + \\ & + & R^*(x', y')O(x', y', d_0) + R(x', y')O^*(x', y', d_0) \end{array} \tag{2.7}$$

In the Eq. (2.7) we see three terms, also called diffraction order terms. The zero order term, indicated by $Q(x', y', d_0)$ is given by

$$Q(x', y', d_0) = \left|O(x', y', d_0)\right|^2 + \left|R(x', y')\right|^2 \tag{2.8}$$

while the other two orders, noted by $H^{+1}(x', y', d_0)$ and $H^{-1}(x', y', d_0)$, are called +1 order (or real order) and -1 order (or conjugate order)

$$\begin{array}{rcl} H^{+1}(x', y', d_0) & = & R^*(x', y')O(x', y', d_0) \\ & = & a_R \left|O(x', y', d_0)\right| \exp\left\{j \arg\left[O(x', y', d_0)\right]\right\} \times \\ & \times & \exp\left\{-j2\pi\left(u_R x' + v_R y'\right) - j\Omega\left(x', y'\right)\right\} \end{array} \tag{2.9}$$

and, it is simple to note that $H^{-1}(x', y', d_0) = \left\{H^{+1}(x', y', d_0)\right\}^*$. Finally, the Eq. (2.7) can be rewritten as

$$H(x', y', d_0) = Q(x', y', d_0) + H^{+1}(x', y', d_0) + H^{-1}(x', y', d_0) \quad (2.10)$$

2.2 Digital recording

In DH, the hologram is recorded with a matrix of pixels. Each pixel induces a sampling of the hologram and also a spatial integration due to its extended surface. Generally, the detector includes $M \times N$ pixels of pitches p_x and p_y, each of them sized $\Delta_x \times \Delta_y$. Therefore, the recorded hologram is [61]

$$H_p(kp_x, lp_y, d_0) = \left[H(x', y', d_0) \otimes \Pi_{\Delta_x,\Delta_y}(x', y')\right]_{(kp_x,lp_y)} \quad (2.11)$$

where $\Pi_{\Delta_x,\Delta_y}(x', y')$ is called pixel function

$$\Pi_{\Delta_x,\Delta_y}(x', y') = \begin{cases} \frac{1}{\Delta_x\Delta_y} & \text{if } \|x'\| \leq \Delta_x/2,\ \|y'\| \leq \Delta_y/2 \\ 0 & \text{otherwise} \end{cases} \quad (2.12)$$

Therefore, we can rewritten the Eq. (2.10) in digital form as

$$\begin{array}{rcl} H_p(kp_x, lp_y, d_0) & = & Q_p(kp_x, lp_y, d_0) \\ & + & H_p^{+1}(kp_x, lp_y, d_0) + H_p^{-1}(kp_x, lp_y, d_0) \end{array} \quad (2.13)$$

where the three diffraction terms are the discrete versions of the terms given in Eq. (2.8) and Eq. (2.9) obtained by the convolution with the pixel function (2.12).

2.2.1 Digital holograms recorded in microscope configuration

Quantitative phase-contrast microscopy (QPM) is a highly demanding experimental process used in various disciplines. Among several that can be used, two major categories exist for full-field, quantitative phase microscopy. One of these is DH [62], which is used, for example, for silicon microelectromechanical system (MEMS) structures, for biological objects [63] and for microfluidics [64]. The QPM is obtained conceptually by subtraction of two phase maps via optical [65] synthetic [66] method, in a manner resembling holographic interferometry [67].

In this section it shown the recording step for a particular MEMS, reported in Figure 2.2 (a), and for an in-vitro cell, reported in Figure 2.3 (a). In order

to compute the phase map (that is shown in the section 2.4.3), two different digital holograms of both MEMS (see Figure 2.2 (b,c)) and cell (see Figure 2.3 (b,c)) are acquired, in the first case in reflection mode and in the other case in transmission mode, by means of a Mach-Zehnder interferometric microscope, superposition unit of which is shown in Figure 2.4. The setup is composed by the laser with wavelength $\lambda = 532nm$, and the microscope objective (MO) with a focal length $f = 9.0mm$. The CCD detector has 1024×1024 square pixels, the size of which is $p_x = p_y = 6.7\mu m$ and the recording distance for the MEMS is $d_0 = 205mm$, while for the cell is $d_0 = 100mm$. Note that, in order to isolate the in-vitro cell under analysis, holograms of different parts of the sample are recorded. The size of these holograms are 256×256 pixels.

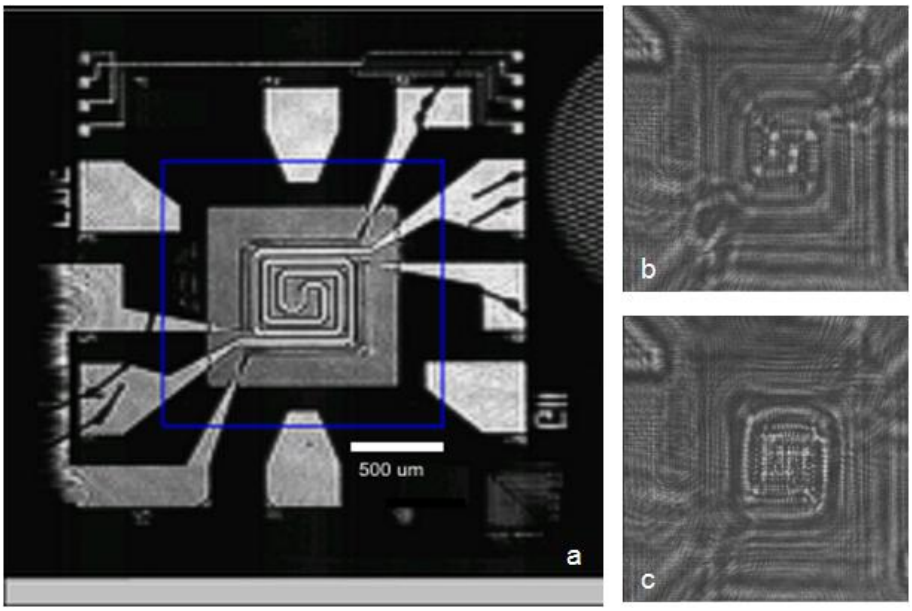

Figure 2.2: (a) Microscopic photo of the MEMS. (b,c) are two recorded holograms of (a) in different experimental conditions

In addition to the QPM, many other applications can be made of digital holograms acquired in microscope configuration, the most of which are based on the property of this kind of digital holograms and its numerical reconstructions. This last aspect will be clarified in the section 2.4.1.

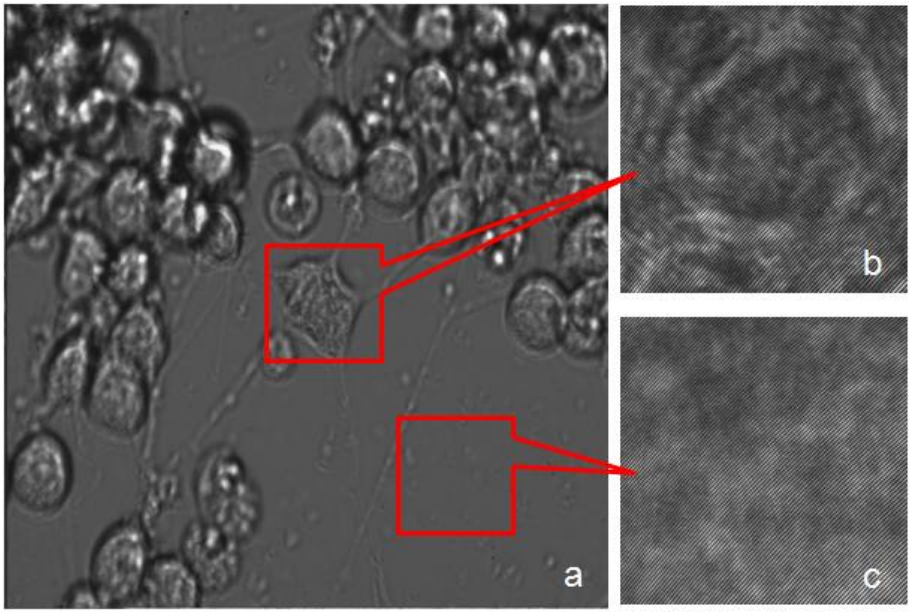

Figure 2.3: (a) In-vitro cell's photo in white light. (b,c) are two recorded holograms of (a) taken in different location

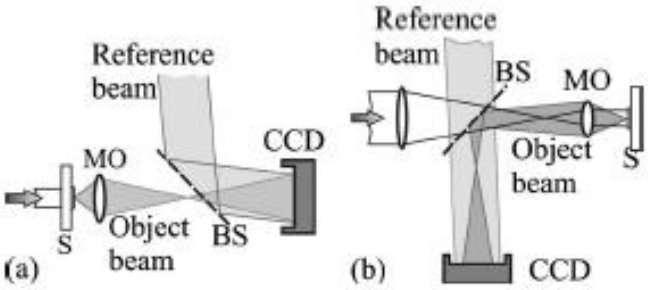

Figure 2.4: Superposition unit of the microscope DH setup in (a) transmission mode and (b) reflection mode: S, sample; BS, beam splitter; MO, microscope objectives.

2.2.2 Digital holograms recorded in lensless configuration

The lensless configuration is typically used to acquire digital holograms of macro objects. In fact no lens is needed to magnify the objects, as shown by the acquisition setup in Figure 2.5 This kind of holograms are suitable to

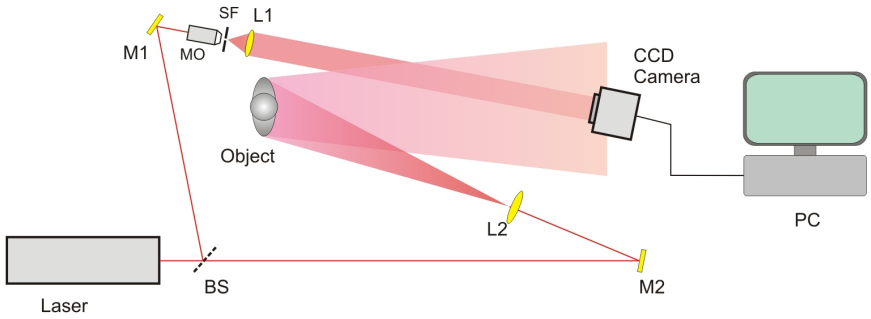

Figure 2.5: Setup for recording the holograms of astronaut puppet and Venus statuettes

holographic displays [57], that have the unique advantage of representing all possible visual depth cues, autostereoscopically (without glasses), with both vertical and horizontal parallax, giving an appropriate medium for unlimited simultaneous viewers at arbitrary viewing positions, and without the potentially nausea-inducing accommodation-vergence rivalry inherent in modern stereoscopic 3D cinema. Several macro-objects can be record with this unit, depending on the dimensions of the objects under consideration. Typically it uses a laser with visible wavelength such as $\lambda = 532nm$. Instead, the recording of objects with size of tens of centimeters is obtained through the same unit shown in Figure 2.5 but using an infrared laser [68], i.e. $\lambda = 10.6\mu m$. In this section two object are considered, the first one is a puppet of astronaut (Figure 2.6), about $3cm$ high, and the other one is a statuette of Venus (Figure 2.7), about $20cm$ high, whose holograms are acquired with visible laser and infrared laser respectively. Another difference in the used setups is the resolution of the detectors. In fact, the recorded hologram of the astronaut puppet is composed by 1024×1024 pixels, with a recording distance $d_0 = 790mm$, by using a CCD camera with pixel size $4.4\mu m \times 4.4\mu m$, while the recorded hologram of the Venus statuette is 640×480 pixels $25\mu m \times 25\mu m$ in size at the recording

distance $d_0 = 490mm$. In addition, in the recording step, a spherical reference wave, with curvature radius $r = 450mm$, is used for the Venus hologram. The reference beam, in this case, can be written as $W(x, y, -r)$ where $W(\cdot)$ is the function defined in Eq. (2.5).

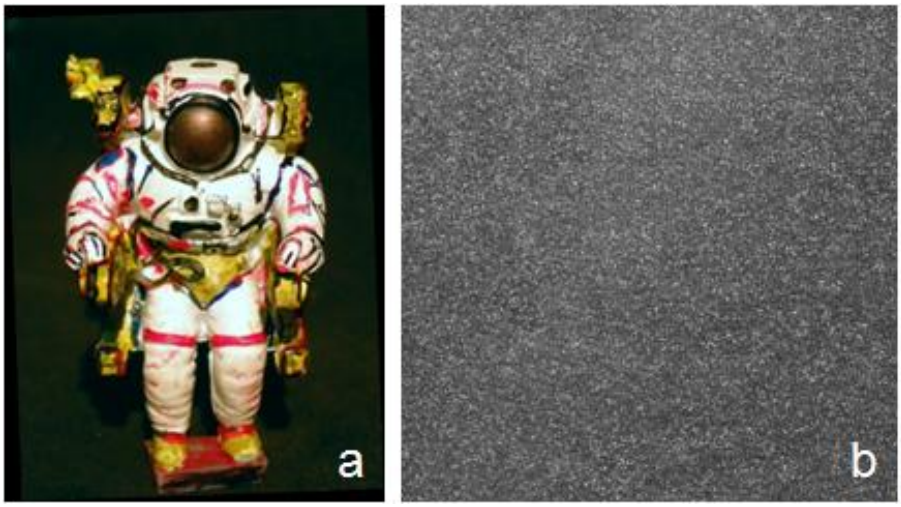

Figure 2.6: (a) Photo of the puppet of astronaut. (b) is the recorded hologram of (a)

2.3 Image formation

According to the diffraction theory, the diffracted fields in the three diffraction orders at any arbitrary distance d from the recording plane can be computed with $(K, L) \geq (M, N)$ data points by evaluating the discrete version of Fresnel integral used in Eq. (2.3). Because the Fresnel transform is proportional to a Fourier transform, as shown in Eq. (2.4), the numerical Fresnel transform will be proportional to the Discrete Fourier Transform ($\mathcal{DFT}$). Therefore, without loss of generality, we can write the numerical diffracted field at distance d as

$$F_R(X, Y, d) = Z(X, Y, d)\mathcal{DFT}\left\{H_p(kp_x, lp_y, d)W(kp_x, lp_y, d)\right\} \quad (2.14)$$

Because the ($\mathcal{DFT}$) operator is linear, we can replace the Eq. (2.13) in the

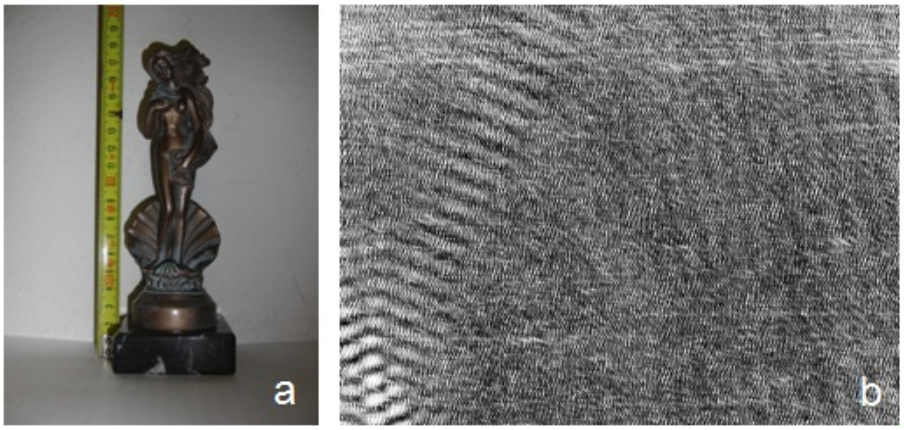

Figure 2.7: (a) Photo of the statuette of Venus. (b) is the recorded hologram of (a)

Eq. (2.14) obtaining

$$F_R(X,Y,d) = A(X,Y,d) + F_R^{+1}(X,Y,d) + F_R^{-1}(X,Y,d) \tag{2.15}$$

where $A(X,Y,d)$, $F_R^{+1}(X,Y,d)$ and $F_R^{-1}(X,Y,d)$ are the discrete Fresnel transform of zero order, +1 order and -1 order respectively. When the distance d corresponds to the in-focus distance, i.e. $d = -d_0$, the Eq. (2.15) is called the *image reconstruction*. Note that, using the properties of $\mathcal{DFT}$, the -1 order can be obtained from the +1 order by the relation

$$F_R^{-1}(X,Y,-d) = \{F_R^{+1}(-X,-Y,d)\}^* \tag{2.16}$$

Still, the zero order term transports a redundant information about the recorded object. Typically, it can be suppressed using different techniques. There are several methods based on prior information about the object and are typically iterative algorithms [69]. Other methods don't use any information, but in these cases the zero order term is only reduced. The most used of them is the filter using High-pass kernel [70]. Finally, supposing that the zero order term was reduced or suppressed and considering the Eq. (2.16), we will focus only on the +1 order. In [58] is demonstrated that the +1 order can be obtained as

$$\begin{aligned} F_R^{+1}(X,Y,d) &= K \times F(-X\tfrac{d_0}{d}, -Y\tfrac{d_0}{d}) \otimes \Pi_{\Delta_x,\Delta_y}(X,Y) \otimes \\ &\otimes \tilde{W}_{ab}(X,Y) \otimes \tilde{W}_d(X,Y) \otimes \tilde{W}_{NM}^*(X,Y) \otimes \\ &\otimes \delta\left(X + \lambda u_R d, Y + \lambda v_R d\right) \end{aligned} \tag{2.17}$$

This relation indicates that the reconstructed object is related to the real one by a convolution relation with different contribution. The first term is the pixel function, the second is due to aberrations of the reference wavefront, i.e. if $\Omega(x', y') = 0$ then $\tilde{W}_{ab}(X, Y) = \delta(X, Y)$, the third is due to the focusing error, i.e. if we consider the in-focus reconstruction distance $d = -d_0$, $\tilde{W}_d(X, Y) = \delta(X, Y)$, the fourth is the filtering function of the 2D ($\mathcal{DFT}$) and it is due to the finite size of the recording [71], [72], [73] and the last convolution term is a localization function in the reconstructed field [61]. Moreover K includes irrelevant constants and phase terms. The Eq. (2.17) can be also written in the general form given in Eq. (2.1) by introducing the impulse response function of the holographic process

$$\begin{array}{rcl} T(X,Y) & = & K \times \Pi_{\Delta_x,\Delta_y}(X,Y) \otimes \tilde{W}_{ab}(X,Y) \otimes \\ & \otimes & \tilde{W}_d(X,Y) \otimes \tilde{W}^*_{NM}(X,Y) \otimes \\ & \otimes & \delta\left(X + \lambda u_R d, Y + \lambda v_R d\right) \end{array} \tag{2.18}$$

that is called the resolution function of the digital Fresnel holography.

2.3.1 Noise components

The description of the image formation, given in the previous section, does not consider the real situation of recording. In fact, in each real acquisition system, always there are some contributions of noise that corrupt the recorded data. In order to consider the presence of noise in digital holograms, firstly we rewrite the Eq. (2.10) as follows

$$H(x', y', d_0) = Q(x', y', d_0) + 2a_R \left|O(x', y', d_0)\right| \cos\left[\varrho(x', y', d_0)\right] \tag{2.19}$$

where we have set

$$\varrho(x', y', d_0) = \arg\left[O(x', y', d_0)\right] - 2\pi\left(u_R x' + v_R y'\right) - \Omega\left(x', y'\right). \tag{2.20}$$

The hologram intensity is normally corrupted by a mixture of speckle noise [74],[75],[76] $n_s(x', y')$, and an additive Gaussian noise $n_a(x', y')$ and Eq. (2.19) becomes

$$\begin{array}{rcl} \tilde{H}(x', y', d_0) & = & Q(x', y', d_0) + 2a_R \left|O(x', y', d_0)\right| \times \\ & \times & \cos\left[\varrho(x', y', d_0) + n_s(x', y')\right] + n_a(x', y') \end{array} \tag{2.21}$$

Obviously, repeating the full process of the image formation on the recorded holograms modeled by Eq. (2.21), the image reconstruction will be corrupted by noise.

2.4 Numerical reconstruction

The digital recorded holograms are reconstructed in the image plane using Eq. (2.22). However, to numerically manage the reconstructed field, it necessary to compute efficiently the image reconstruction and then we compute the $\mathcal{DFT}$ of the holograms using the Fast Fourier Transform ($\mathcal{FFT}$)algorithm.

$$\begin{aligned} F_R(k'\rho_x, l'\rho_y, d) &= Z(k'\rho_x, l'\rho_y, d)\times \\ &\times \mathcal{FFT}\left\{\tilde{H}_p(kp_x, lp_y, d)W(kp_x, lp_y, d)\right\} \end{aligned} \tag{2.22}$$

The Eq. (2.22) shows the numerical diffracted field obtained by the reconstruction with $\mathcal{FFT}$. Recalling that the size of digital recorded holograms is $M \times N$, while the size of the diffracted field is $L \times K$, in general results $(K, L) \geq (N, M)$ but typically equal dimensions are used. The quantities ρ_x, ρ_y are the pitches in the reconstruction plane and they are related to the pitches in the hologram plane by the following equations

$$\begin{cases} \rho_x = \frac{\lambda d_0}{N p_x} \\ \rho_y = \frac{\lambda d_0}{M p_y} \end{cases} \tag{2.23}$$

In the following are computed the numerical reconstructions of the objects shown in the sections 2.2.1 and 2.2.2. In order to show the reconstructions we compute both the amplitude and phase maps of diffracted fields. As told in the section 2.3, at each holograms is applied an high-pass convolution kernel able to suppress the zero-order term. A particular considerations is necessary for the numerical reconstruction of the hologram of the Venus statuette. As mentioned in the section 2.2.2, this digital holograms was acquired using a spherical reference beam and in this case the reconstruction formula, given in Eq. (2.22), becomes

$$F_R(X, Y, d) = Z(X, Y, d)\mathcal{DFT}\left\{H_p(kp_x, lp_y, d)W(kp_x, lp_y, d_{IR})\right\} \tag{2.24}$$

The reconstruction distance in Eq. (2.24) is given by $d_{IR} = \frac{r-d}{rd}$ and results that

$$W\left(kp_x, lp_y, \frac{r-d}{rd}\right) = W(kp_x, lp_y, d)W(kp_x, lp_y, -r) \tag{2.25}$$

2.4.1 Amplitude reconstruction

Firstly we consider the in-focus distance given by $d = -d_0$, i.e. for the holograms recorded in microscope configuration $d = -205mm$ for MEMS and

$d = -100mm$ for in-vitro cell. In Figure 2.8 are shown the amplitude reconstructions for the cases of digital holograms recorded in microscope configuration.

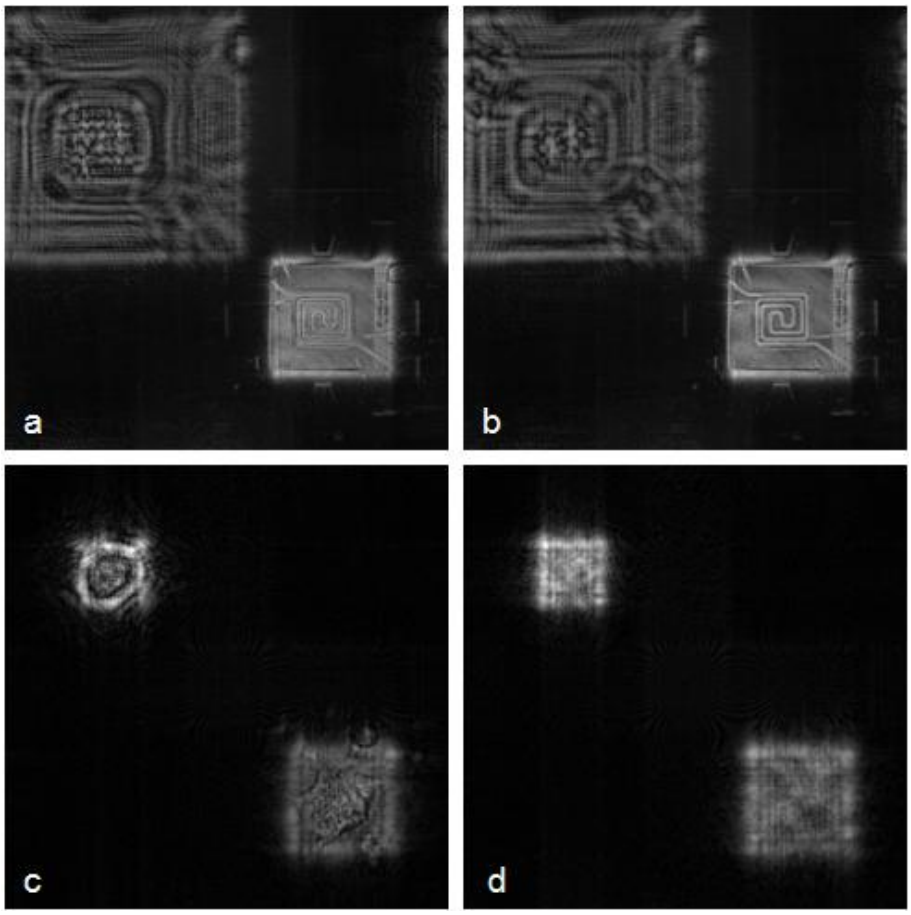

Figure 2.8: (a,b) are the amplitude reconstructions of holograms of MEMS, while (c,d) are the amplitude reconstructions of holograms of in-vitro cell

Applying the relation (2.16) we obtain the in-focus reconstruction for the -1 order at distance $d = d_0$ for both examples (Figure 2.9).

For both holograms of astronaut and Venus are repeated the same operations and their amplitude reconstructions are shown in Figure 2.10. There-

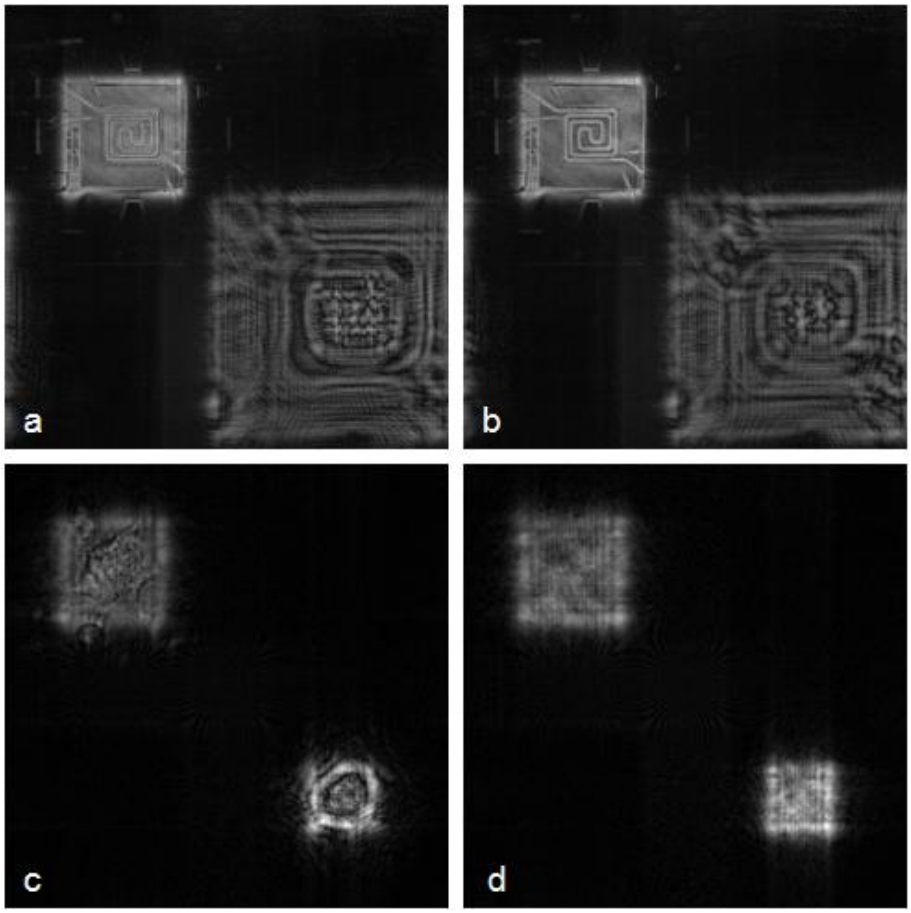

Figure 2.9: (a,b) are the amplitude reconstructions of holograms of MEMS with focus on the -1 order, while (c,d) are the amplitude reconstructions of holograms of in-vitro cell with focus on the -1 order

fore,for the hologram of astronaut, we have $d = -790mm$ (focus on +1 order) and $d = 790mm$ (focus on -1 order). Instead, as has been said in the previous section, the hologram of Venus is reconstructed according to the Eq. (2.24), therefore we consider both in-focus distance $d = -490mm$ and curvature radius of the spherical reference wave $r = -450$ for the +1 order, while $d = 490mm$, $r = 450mm$ for the -1 order).

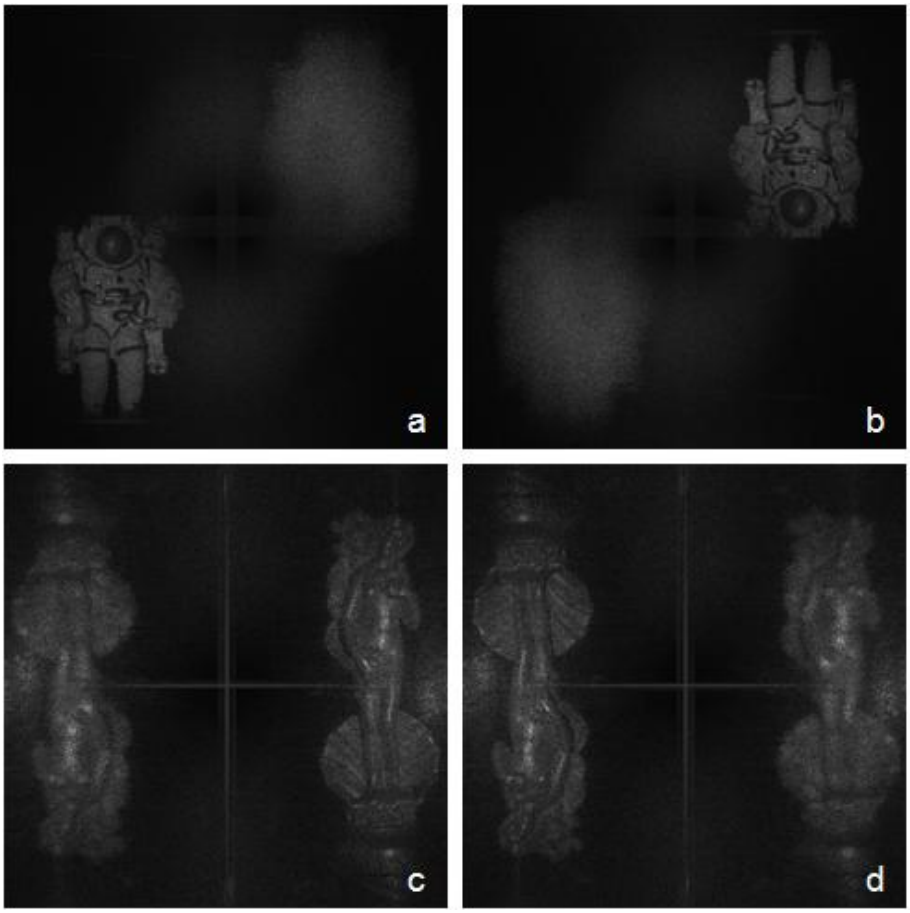

Figure 2.10: (a,c) are the amplitude reconstructions of holograms with focus on the +1 order, while (b,d) are the amplitude reconstructions of holograms with focus on the -1 order

As shown in all amplitude reconstructions, the relation (2.16) is equivalent

to the rotation of 180° of the complex reconstructed fields. Finally, exist another digital reconstruction distance for the hologram recorded in microscope configuration exist, called Back Focal Plane (BFP) distance, that has a great interest in several applications [77],[78]. At this distance, the complex wavefield is proportional to the $\mathcal{FT}\ F(\cdot,\cdot)$ of the complex amplitude of the wave at an input plane, regardless of its distance d from the lens according to the equation [79]

$$g(X,Y,d_{BFP}) = S_l S_d F\left(\frac{X}{\lambda f}, \frac{Y}{\lambda f}\right) \tag{2.26}$$

where $S_d = \exp\left\{j\pi\left(X^2+Y^2\right)\frac{(d-f)}{\lambda f^2}\right\}$ is a phase factor depending on d, $S_l = \frac{j}{\lambda f}\exp\left\{-j4\pi\frac{f}{\lambda}\right\}$. and f is called the focal length. For the considered examples, it results $d_{BFP} = -615mm$ for the MEMS and $d_{BFP} = -425mm$ for the in-vitro cell. In Figure 2.11 are reported the amplitude BFP reconstructions for both cases in which the terms that assume the minimum spatial occupation are the +1 orders.

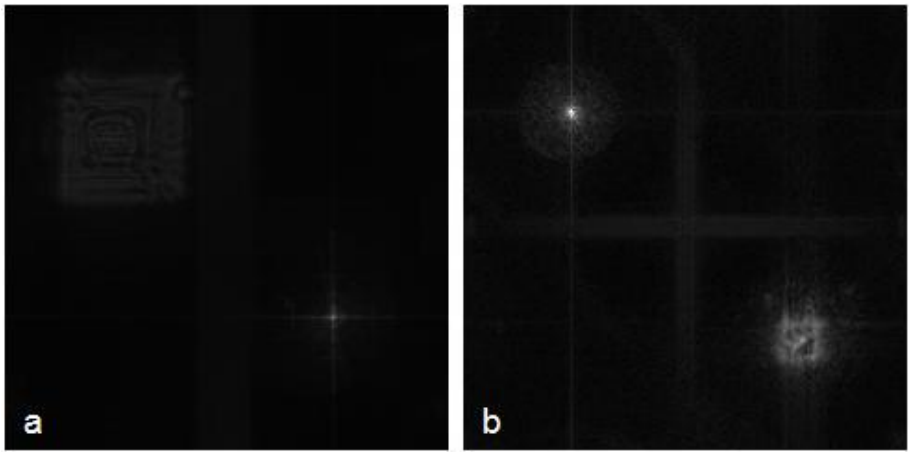

Figure 2.11: (a) is the amplitude BFP reconstructions of holograms of MEMS, while (b) is the amplitude BFP reconstructions of holograms of in-vitro cell

2.4.2 Auto-focusing

The searching and recovery of the correct in-focus distance for the +1 order can be cumbersome and time-consuming for dynamic measurements or scenes in which hundreds of holograms are recorded and where the focus can change in each holographic exposure. Furthermore, the evaluation of the correct in-focus reconstruction distance is subjective, as it is usually judged by the observer. In fact, not always the value of recording distance d_0 is available. When the numerical reconstruction is computed at distance $d \neq -d_0$, in the Eq. (2.17), results $\tilde{W}_d(X,Y) \neq \delta(X,Y)$, i.e. an out-focus numerical reconstruction. Different strategies are necessary to detect the correct focal plane according to the kind of object under investigation and the adopted configuration, i.e., pure phase objects [80], in-line holography [81], scanning holography [82], or for detecting depth of objects in multiple planes [83]. Moreover, an algorithm that maximizes a sharpness metric related to the sparsity of the signal's expansion in distance-dependent waveletlike Fresnelet bases has been found in DH [84] The most popular algorithms to estimate the in-focus distance [85] exploit the cumulated edge detection to quantify the image sharpness. To this aim, the total sum of the gradient, the Laplacian, or the variance of gray-value image distribution is calculated for each distance considered and the maximum value is computed. It is interesting to note that all the methods mentioned have several local maxima points in the range of searching, that can produce a wrong convergence during the optimization stage. Recently [86] an estimation algorithm for the in-focus distance, based on the contrast texture measure model [87], is proposed in order to overcome the wrong convergence of the other well known methods. As a measure of contrast, is an approximation of the Tamura coefficient is used [88]

$$C_\delta = \sqrt{\frac{\sigma(\mathbf{I})}{\langle \mathbf{I} \rangle}} \tag{2.27}$$

where $\sigma(\mathbf{I})$ and $\langle \mathbf{I} \rangle$ represent the image gray-level standard deviation and mean, respectively. The "image", in this case is represented by the numerical reconstruction of hologram, computed at a particular distance δ. This method works well for digital holograms recorded in lensless configuration, while for the digital holograms recorded in microscope configuration it is able to find the BFP distance. The optimization problem for the computation of the in-focus distance is the following

$$\hat{d} = \arg\max \; C_\delta \quad \text{subject to} \quad \delta \in \Delta \tag{2.28}$$

where Δ is the interval of the research. The application of this algorithm on the astronaut and MEMS is showed in the Figure 2.12.

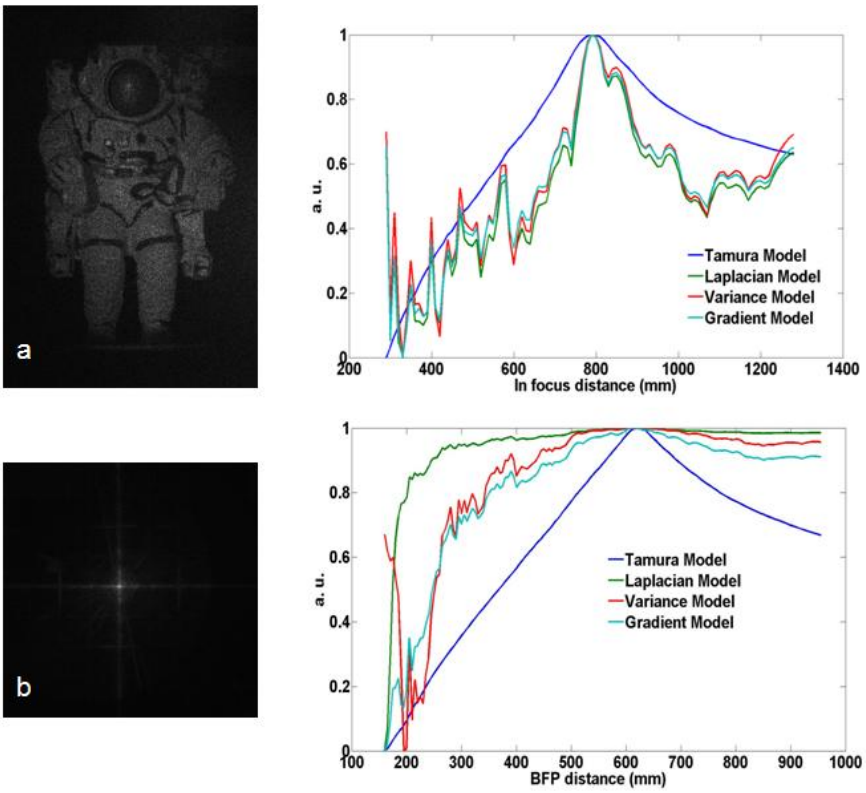

Figure 2.12: Results of the autofocusing algorithm for the estimation of the in-focus distance for the astronaut (a) and the BFP distance for the MEMS (b)

It is possible to note that, even if you chose a range of research that does not belong to the correct in-focus distance, it can easily understand how to shift this range by increasing/decreasing the coefficient. In fact, if the coefficient increases, the right extreme must be extended, while, if the coefficient decreases, the left extreme must be reduced.

2.4.3 Phase reconstruction

Finally, in order to complete the analysis on the numerical reconstruction of holograms, we consider the retrieve of the phase map by the subtraction between a digital hologram and its reference holograms, in the Figure 2.13 are shown the phase reconstruction obtained by the holograms of MEMS and in-vitro cell reported in Figure 2.2 and Figure 2.3.

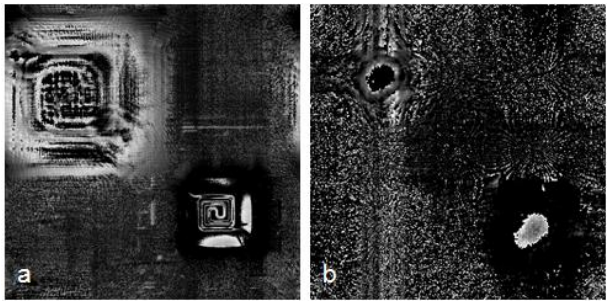

Figure 2.13: (a) is the phase reconstruction of the hologram of MEMS, while (b) is the phase reconstruction of the hologram of in-vitro cell

In order to remove the 2π ambiguity, that in the Figure 2.13 are represented by the spatial jump form black to white and viceversa, the unwrapping process [70], [89] is computed. Obviously, the -1 order cannot be used for phase map analysis because is out of focus. Therefore, the unwrapping algorithm is applied only on the spatial region in which there is the +1 order. In Figure 2.14 is reported the result of the unwrapping applied on the phase maps in Figure 2.13

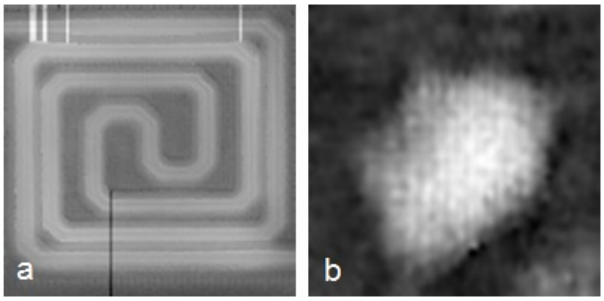

Figure 2.14: Unwrapped phases of holograms of MEMS (a) and in-vitro cell (b).

The phase errors occurred in Figure 2.14(a) are caused by the unwrapping algorithm that is not able to correct all the phase jumps.

Chapter 3

Digital holograms recovery using CS

High resolution holography typically involves dense data acquisition. Several fields of research aim to reduce the amount of recorded data limiting, for example, the acquisition in the area where is present the most information about the signal [90], or using sample illumination [91]. However, these methods suffer from being image-content dependent for a successful implementation. In the recent years, the sensing problem was performed in terms of CS, because, as told in the previous chapters, it is independent of the image content and does not need any feedback loop during the acquisition. The application of CS paradigm in DH is enveloped through two different frameworks. The first framework refers to a noiseless scenario where the CS paradigm is used as a compression method for digital holograms in order to reduce the stored data. In fact, the possibility to recover the sparse signals using few noiseless measurements can be used for represent a digital holograms from few pixels value achieving compression factor around 10-15 preserving all of the information obtained in the recording step. Note that CS is a lossless compression technique that allow to reconstruct perfectly the signal if the number of sample is higher that $2k$ where k is the sparsity of the signal (see Eq. (1.1)). However, other recently lossy compression techniques permit to achieve a compression factor much higher the CS, as shown in [92]. The second framework consider a noisy scenario where degraded measurements at high noise levels in the case of holographic microscopy in low-light conditions. In most of the relevant practical scenarios the knowledge of the noise statistics is not or only partially available. In all these scenarios CS can be

to use as a powerful method to retrieve the digital holograms as also shown [18],[19] thanks to the well-known Lipschitz continuity of the reconstruction method which make the reconstruction algorithm designed for the noiseless measurements robust with respect to the noise. The advantage of using typical CS reconstruction technique instead of the classical bayesian approach is that CS algorithm do not require knowledge of the noise statistics and this make them extremely robust with respect to imperfect knowledge of the noise statistics. Thanks to its robustness to the noise the typical CS reconstruction algorithm can be also used directly as denosing algorithms without exploring its compressing aspect. Until now, the use of CS in DH has been formulated only for the microscopy case [18],[19], without consider other kind of possible recorded objects as, for example, the digital holograms recorded in lensless configuration, described in the section 2.2.2. This chapter describes the results about the application of CS framework in DH as a reconstruction method from randomly undersampled measurements. Therefore, we consider the sensing problem of noisy data for both digital holograms recorded in lensless configuration and digital holograms recorded in microscope configuration proposing a new unified general scheme of the recovery, in order to optimize the recording step. The case of noisy holograms recovery for the optimization of the numerical reconstruction, without consider undersampled measurements but the full recording ones, will be discussed in Chapter 4.

3.1 Nyquist/Shannon sampling theorem in DH

As shown in section 2.2, the recording process is a sampling of an interference pattern consisting of spatial frequencies, the highest of which is given by the largest angle between object and reference wave. The limited resolution of the CCD chip and similar digital devices decides the maximum frequency allowed for sampling and severely restricts the experimental set-up configuration. According to the Nyquist/Shannon sampling theorem [21],[22],[59],[93] each period must be recorded by at least two detector elements. If Λ is the fringe spacing and d_p the detector pitch (centre-to-centre spacing between neighbouring detector elements) in one transversal direction, then

$$2d_p \leq \Lambda \tag{3.1}$$

A geometrical evaluation of the angle θ between the object and the reference wave is

$$\Lambda = \frac{\lambda}{2\sin\left(\frac{\theta}{2}\right)} \tag{3.2}$$

Combining Eqs. (3.1) and (3.2) gives

$$\theta \leq 2\arcsin\left(\frac{\lambda}{2d_p}\right) \tag{3.3}$$

where $f_s = \frac{1}{2d_p}$ is the sampling frequency. This means that, the angular extent of the object, $\theta_{\max}$, in Figure 3.1, must not exceed this limit. In order to use the entire available bandwidth of the recording device, the equal sign in Eq. (3.3) should be used. Another geometrical evaluation shows that if the distance d_0 between the CCD and the object is

$$d_0 \approx \frac{2d_p}{\lambda} D \tag{3.4}$$

then the maximum bandwidth is obtained without violating the sampling theorem. D is the transversal size (height or width) of the object, and small angular values are assumed according to Eq. (3.3)

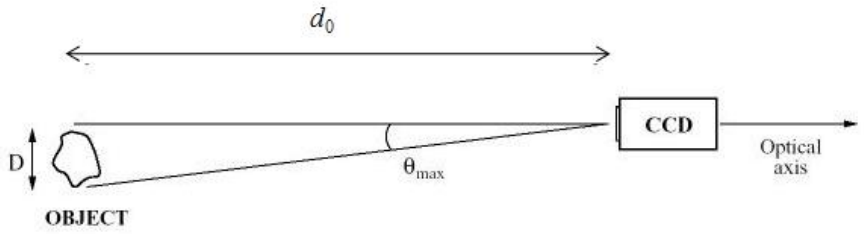

Figure 3.1: Schematic view of the angular extent of the object: θ is the angular extent of the object and the maximum angle between object and reference wave; d_0 is the distance along the optical axis between the CCD chip and the object; D is the transversal size of the object, normal to the optical axis.

Using the CS paradigm it is possible to reduce the limit imposed by Eq. (3.3). In fact, as consequence of CS theory, when a generic signal $\mathbf{x} \in R^n$

admits a sparse representation, is possible to reduce the number of samples, needed to reconstruct exactly the signal, below the sampling theorem's limit. In the following sections, we apply the CS framework on digital holograms recorded in both lensless and microscope configurations, providing an unified procedure, able to recover the numerical reconstruction from randomly undersampled measurements for both cases.

3.2 Sparse representation of digital holograms

In order to obtain an unified recovery algorithm, we must find a suitable sparse representation available for digital holograms recorded in both lensless and microscope configurations. Recalling that, in the field of image processing, CS exploits the fact that most images present some compact structure and redundancy and was previously reported in magnetic resonance imaging acquisition [94] and single-pixel imaging [95]. In these cases the representation of the image in a sparse domain is obtained principally by a multiscale wavelet transform and the computation of image gradient. The same approaches are used in DH microscopy. Therefore the sparse hologram is obtained from wavelet transform or gradient computation. Figure 3.2 shows an example of the wavelet transform of the digital hologram reported in Figure 2.2(b), and the gradient of its in-focus reconstruction, according to [18].

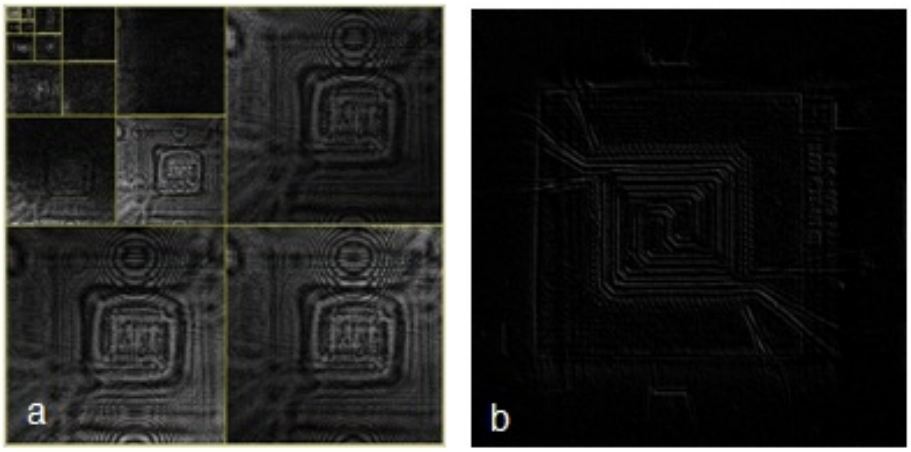

Figure 3.2: Wavelet transform (a) and gradient image (b) for the MEMS. The gradient is computed on the magnification of the +1 order.

Note that, the wavelet transform, computed using 5 decomposition level, don't guarantees an high degree of sparsity, instead the gradient image obtained from the magnification of +1 order of MEMS gives a better results. Moreover, the gradient does not work the same way for the digital holograms recorded in lensless configuration. In fact, as shown in Figure 3.3, there are a very few zero values, and then, for this kind of digital holograms, cannot be applied the recovery algorithm reported in [18].

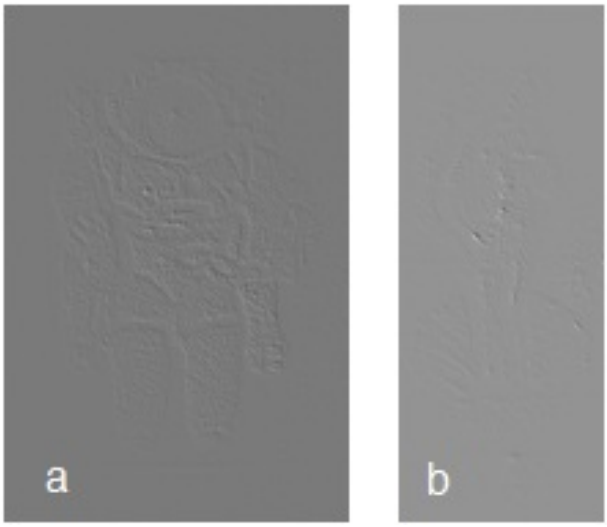

Figure 3.3: Gradient image of astronaut (a) and Venus (b).

However, exists other ways to represent in a sparse form the digital holograms. First of all, we must consider that each real data acquisitions are corrupt by noise, then we consider the sparsity for the noiseless data. From this consideration and recalling that a generic digital hologram presents three diffraction orders in the Fresnel domain, the much intuitively way to obtain the sparse form of the digital holograms is to use the numerical reconstruction.

Figure 3.4 shows a general scheme of image formation for the three diffraction orders and is well clear that the noiseless numerical reconstruction is a sparse signal. In addition, it is considered always the situation of zero-order suppression through high-pass convolution kernel that permits to achieve a much higher degree of sparsity. Therefore, in the follow is considered the Fresnel transform as a basis matrix for the CS.

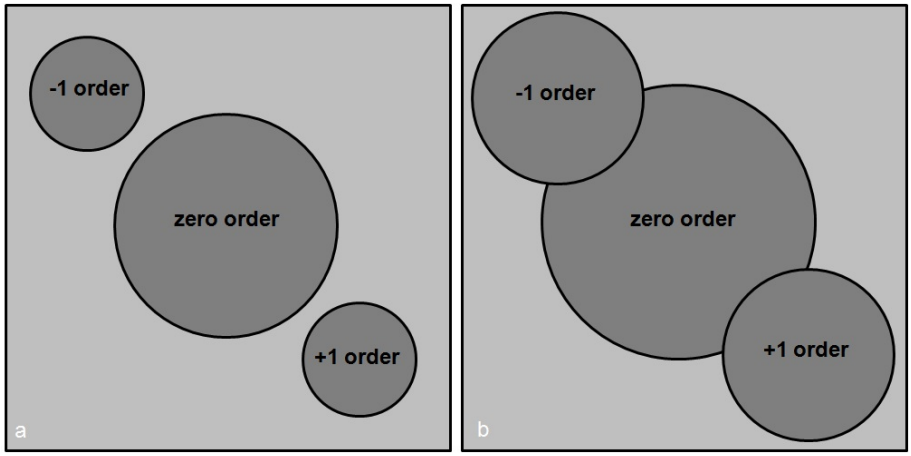

Figure 3.4: Schemes of reconstructed field in off-axis configuration without overlap (a) and with overlap (b)between the diffraction orders

3.3 Recovery of digital holograms using CS

In the section 1.2.4 was present a guideline to choice the sensing matrices for signal recovery optimization. Obviously, the same considerations can be adopted for digital holograms, but the size of sensing matrix depend of the sparsity transform used. In fact if it uses the l_1 minimization of discrete wavelet transform ($\mathcal{DWT}$) or gradient function, that is called Total Variation ($\mathcal{TV}$) minimization, $\mathcal{TV}(\mathbf{x}) = \|\text{grad}(\mathbf{x})\|_1$, the choice of number of measurements (row dimension m of sensing matrix $\mathbf{\Phi}$) becomes a degree of freedom. In addition, because the recorded digital holograms are corrupted by noise, we should use a noisy recovery signal optimization given in Eq. (1.12). The presence of the parameter ϵ in this optimization problem becomes another degree of freedom because it depends of the noise variance, that is an additional information that not always is available. Therefore, in the first, consider the noiseless formulation given in Eq. (1.10) and rewrite it as a holograms recovery problem. Given the measurements $\tilde{\mathbf{h}} = \text{vec}(\tilde{\mathbf{H}})$, that is a MN-vector obtained from the recorded digital hologram $\tilde{\mathbf{H}}$, which has dimension $M \times N$,

$$\widehat{\mathbf{v}} \;=\; \arg\min \;\; \|\mathbf{v}\|_1 \quad \text{subject to} \quad \Phi\mathbf{v} = \Phi \mathrm{F}_\delta \tilde{\mathbf{h}} \tag{3.5}$$

with $\mathbf{v}$ is the sparse representation of the digital hologram through the Fresnel transform $\mathbf{F}_\delta$, valued at distance δ. In order to solve the optimization problem

(3.5), we use a solver called "*SolveBP.m*" that is a MATLAB script implementing the BP method, available online at website http://sparselab.stanford.edu/. The algorithm is applied on all examples given in sections 2.2.1 and 2.2.2. Several values of dimension m of sensing matrix are considered, each of them chosen as a fractions of the original data size $n = MN$. In particular, we choose $m = \{n/16, n/32, n/64\}$. In the next two sections are shown the results of the recovery problem from undersampled measurements given in (3.5), while the case of noisy measurements is treated in the following chapter.

3.3.1 Recovery of lensless holograms

For this kind of digital holograms, the Fresnel transform calculated at in-focus distance, i.e. $\delta = d$, is chosen as basis matrix for CS recovery. The recovered amplitude reconstructions of the digital holograms of both astronaut (Figure 3.5) and Venus (Figure 3.6) are computed at different values of m as indicated in the previous section. In order to quantify the effectiveness of recovered numerical reconstructions, is computed the residual images between the recovered undersamples ones and original ones and they are shown in the Figure 3.5(b,d,f) and Figure 3.6(b,d,f). Also we compute a numerically residual as

$$E = \frac{\left\| \mathbf{F}_d(\hat{\mathbf{h}} - \tilde{\mathbf{h}}) \right\|_2}{\left\| \mathbf{F}_d \tilde{\mathbf{h}} \right\|_2} \tag{3.6}$$

where $\tilde{\mathbf{h}}$ is the recorded digital hologram while $\hat{\mathbf{h}}$ is the recovered one. The Table 3.3.1 shows a summary of the residual E computed for both astronaut and Venus.

	m=n/64	**m=n/32**	**m=n/16**
Astronaut	0.5787	0.2623	0.0299
Venus	0.6461	0.1929	0.0267

Table 3.1: Calculation of the residual E for the astronaut and Venus holograms

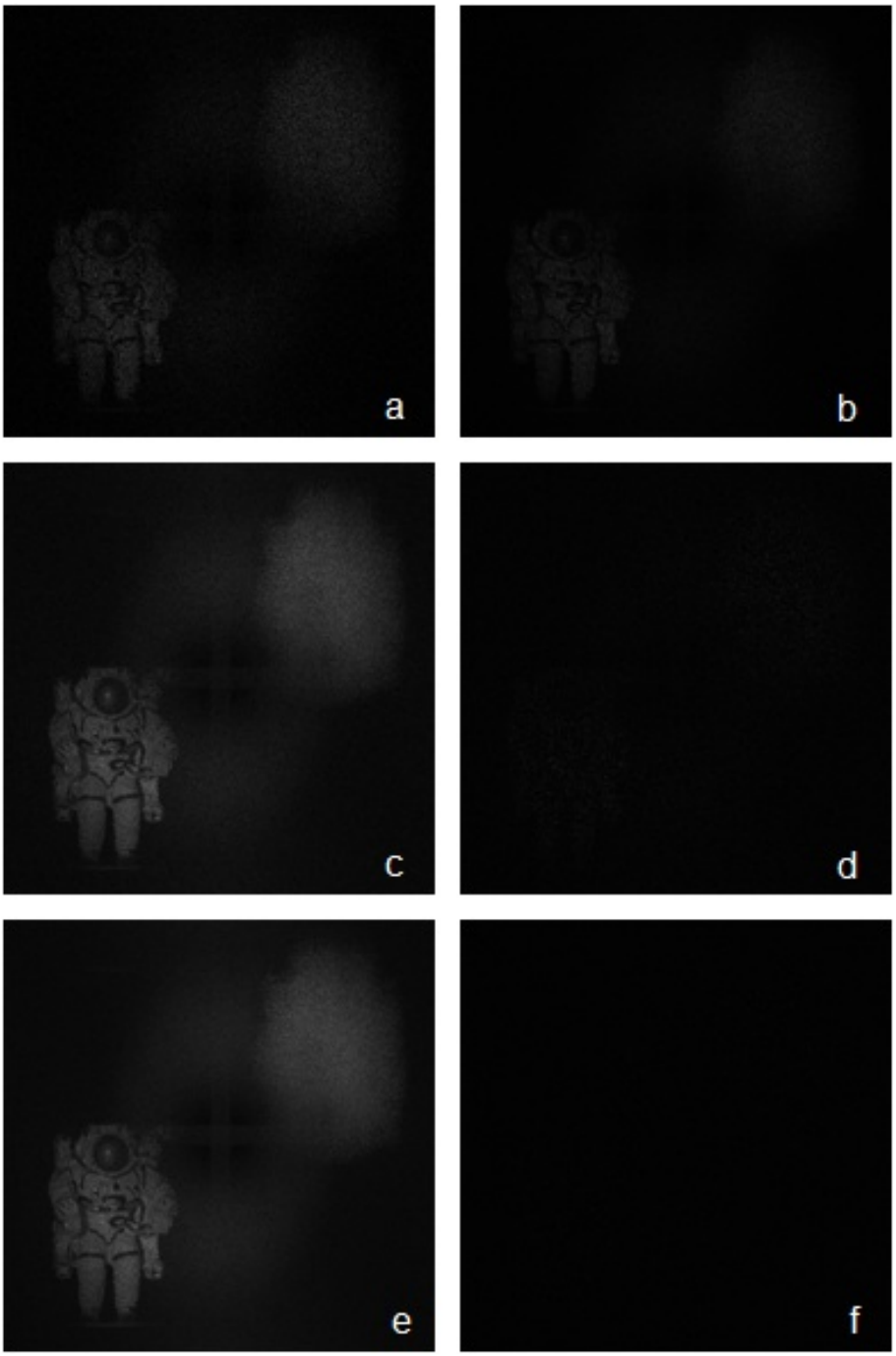

Figure 3.5: Results of recovery algorithm on the astronaut with m = n/64(a), m = n/32(c) and m = n/16(e) and relatively residual images (b,d,f)

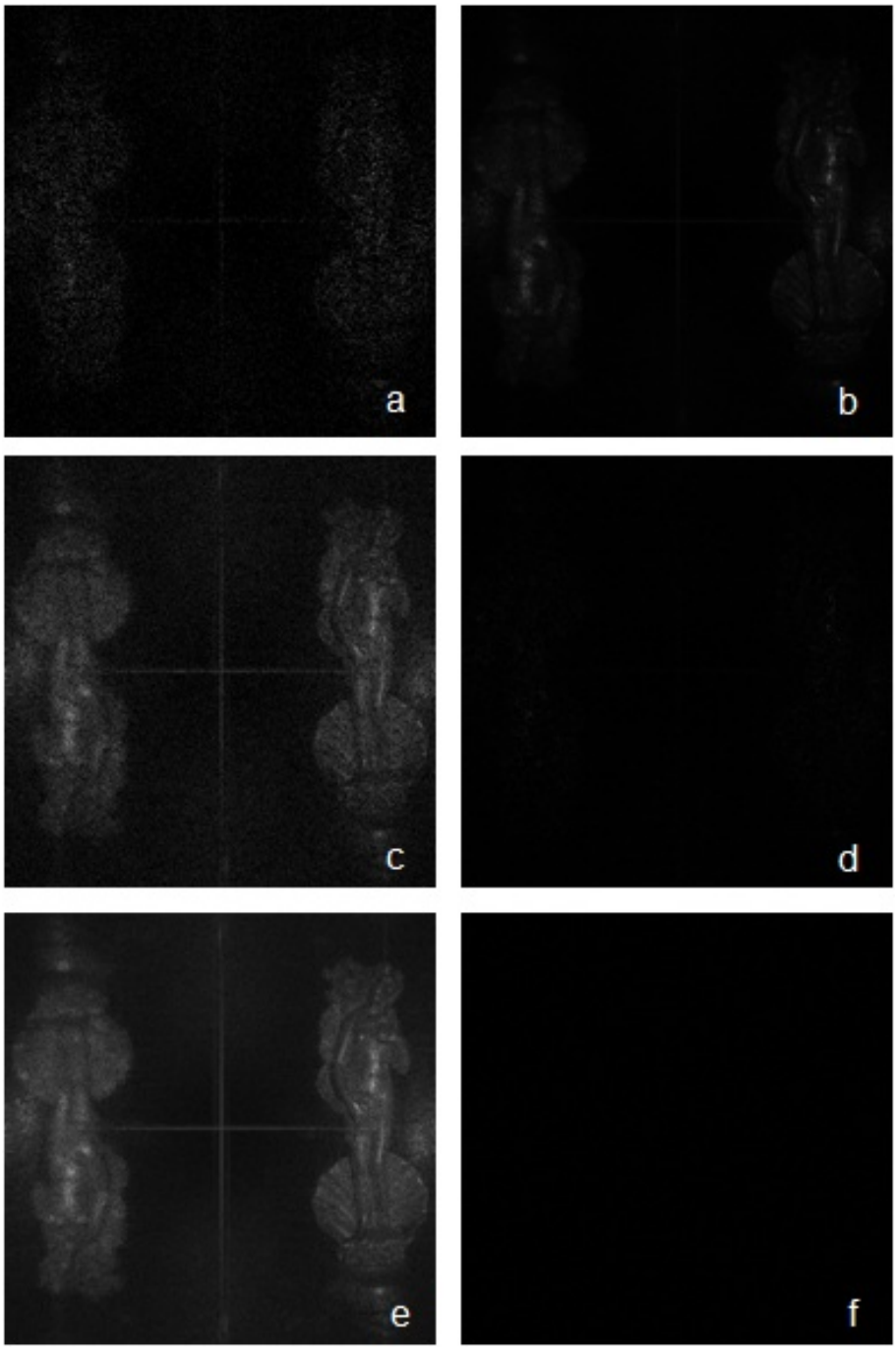

Figure 3.6: Results of recovery algorithm on the Venus with m = n/64(a), m = n/32(c) and m = n/16(e) and relatively residual images (b,d,f)

3.3.2 Recovery of microscope holograms

Also in this case, we set $\delta = d$ and the results of the recovery algorithm is shown in the Figure 3.7 and Figure 3.8 for MEMS and in-vitro cell respectively. However, we consider only the holograms reported in Figure 2.2(b) and Figure 2.3(b) because the other two holograms are the reference holograms of these ones.

Observing the figures is clear that for the holograms recorded in microscope configuration, don't get the same quality in terms of recovery with respect the lensless ones and this is related to the fact that the degree of sparsity of these numerical reconstructions is lower than the lensless case. In other word, with the same ratio $\frac{m}{n}$, do not get a perfect reconstruction from undersampled measurements. we could increase the value of m in the recovery stage, but we can overcome this limitation, applying the recovery algorithm on the BFP reconstructions. In fact, as has been said, in this particular reconstruction plane, there is the much higher degree of sparsity. After the recovery in the BFP, the in-focus reconstructions are computed and compared with the equivalent ones, obtained by the recovery in the image plane. The Table 3.3.2 shows this comparison in terms of the residual given in Eq. (3.6)

Figure 3.9(b,d) as well as the values of residual E computed for the BFP reconstructions demonstrate the improvements obtained.

	m=n/64	**m=n/32**	**m=n/16**	**m=n/16 BFP**
MEMS	0.8032	0.5605	0.2216	0.0366
Cell	0.9371	0.7478	0.3591	0.0618

Table 3.2: Calculation of the residual E for the MEMS and in-vitro cell holograms

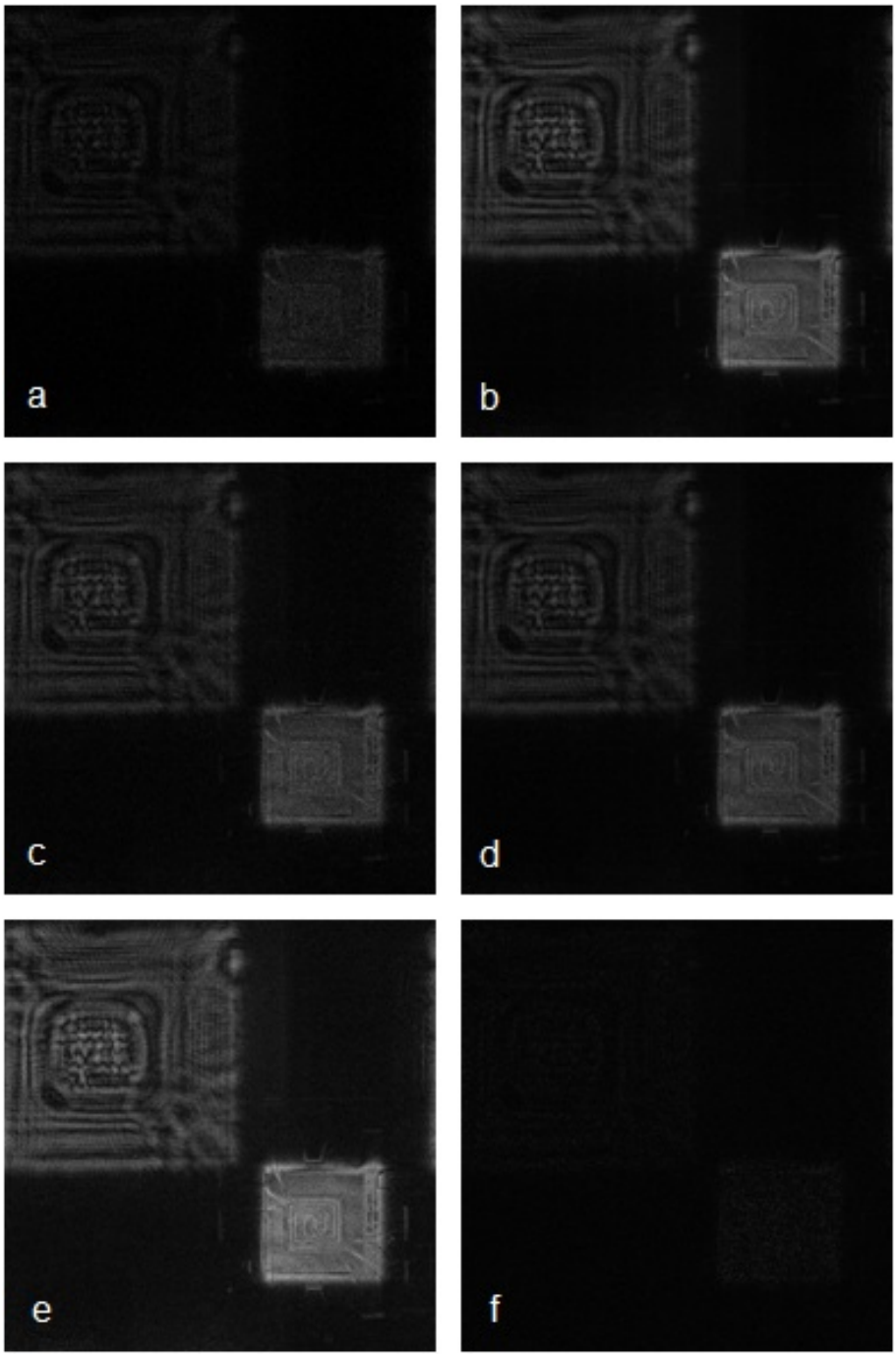

Figure 3.7: Results of recovery algorithm on the MEMS with m = n/64(a), m = n/32(c) and m = n/16(e) and relatively residual images (b,d,f)

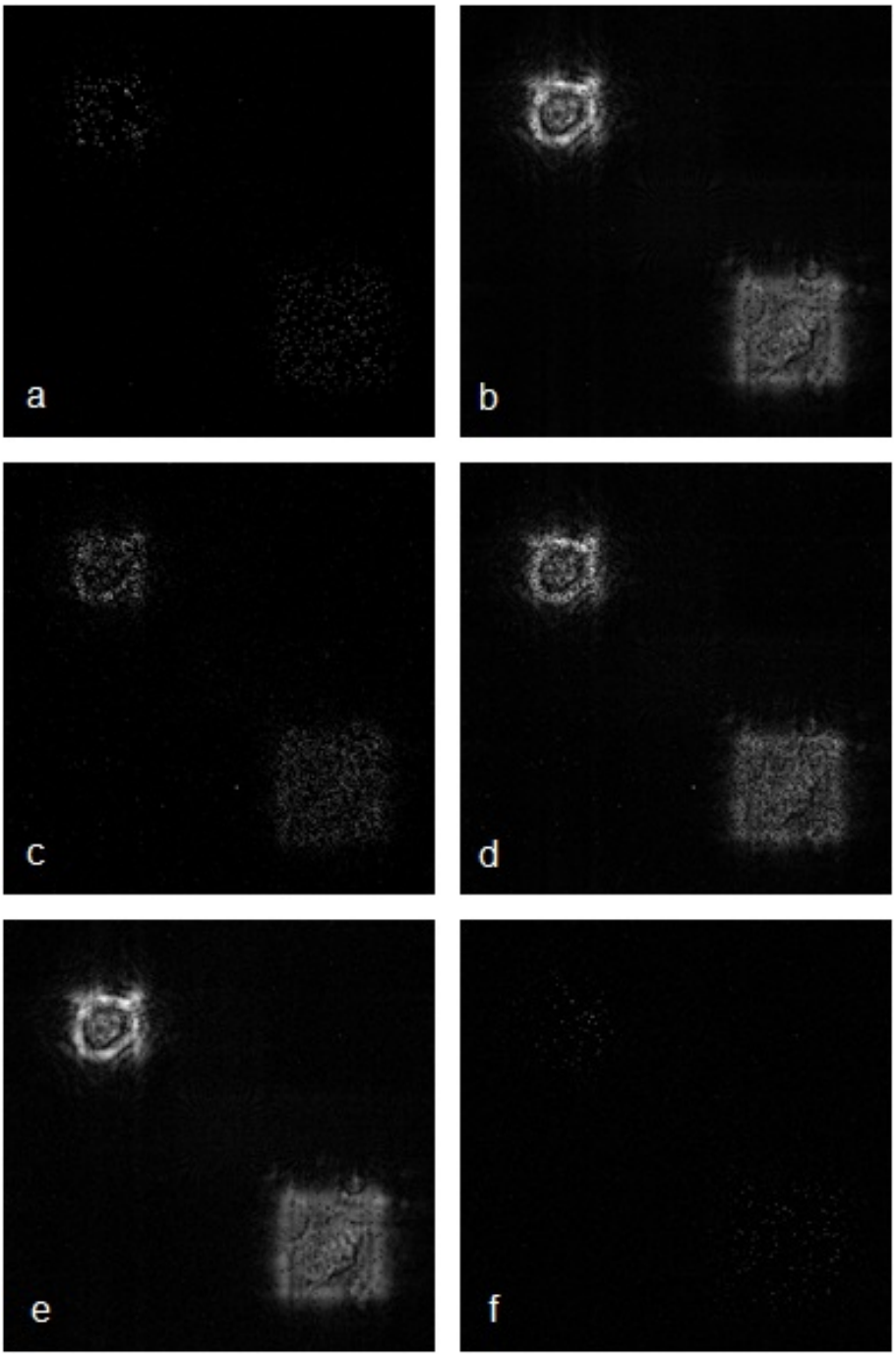

Figure 3.8: Results of recovery algorithm on the in-vitro cell with m = n/64(a), m = n/32(c) and m = n/16(e) and relatively residual images (b,d,f)

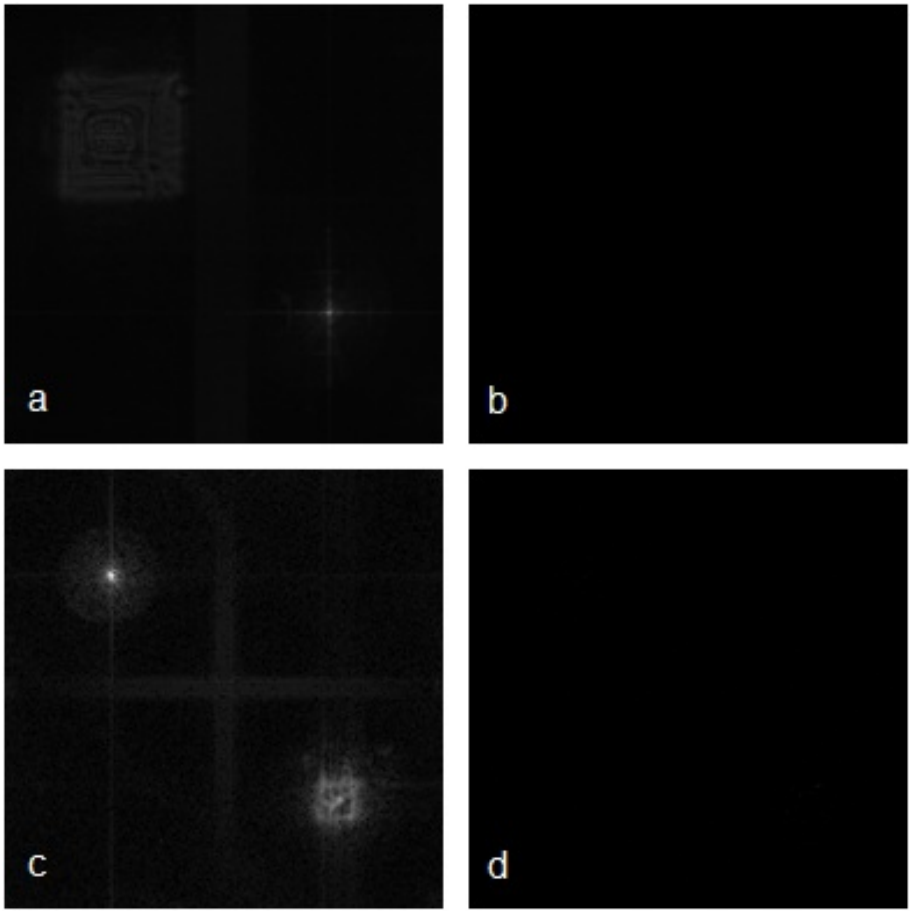

Figure 3.9: Results of recovery algorithm on the MEMS (a) and in-vitro cell (c), with m = n/16(e) in the BFP and relatively residual images (b,d)

Chapter 4

Denoising of digital holograms using CS

As has been said in the previous chapters, in most real-world systems the measurements are likely to be contaminated by some forms of noise. The perfect solution of the noisy signal recovery problem can be obtained using the formulations given in Eq. (1.12) or the BPDN given in Eq. (1.15), in which both recovery of undersampled measurements and denoising is realized. In order to obtain a good reconstruction from noisy measurements the parameter ϵ need to be optimized based usually on the noisy statistics (typically second order statistics) However in most practical scenarios, the statistic characterization of the noise isn't available and typically a way to obtain such knowledge is to estimate the statistics from several measurements of the signal. However, this approach requires that the noise is an ergodic process. In most cases this assumption is not always verified. Furthermore, in our specific setting, i.e. in DH, the digital holograms typically are corrupted by two the components of noise, speckle noise, that is a multiplicative noise, and an additive Gaussian noise (see Eq. (2.21)), hence getting a correct estimate of the second order statistics of the noise is not realistic since we do not knowledge of the second order statistics of the signal and of the speckle noise, and greedy CS reconstruction algorithms, like OMP and StOMP, analyzed in Chapter 3, where the prior knowledge of the noise in not required, reveal as a powerful method to retrieve the digital hologram from its noisy measuraments. In this chapter, we focus on the noisy scenario described above and we propose a new greedy algorithm based on a modification of recovery problem for noiseless data given in Eq. (1.10), without any prior knowledge or estimation about the statistics of

noise. Since the compression properties of the CS techniques applied to DH has been already analyzed numerical in Chapter 3, in this chapter we only focus on the denoising capability of the CS algorithms and on their robustness with respect the lack of knowledge of the noise statistics. This is equivalent to assume the sensing matrix equal to the identity matrix. The proposed algorithm is tested in several cases for both 1D data and 2D data (digital holograms) and compared with two denoising algorithms: a recently greedy algorithm based on CS, described in [96], and a classical Fourier filtering [74]. In the first case, the comparison, given only for 1D signals, starts with the same hypothesis, in the sense that both greedy algorithms work without prior knowledge about the statistics of noise. In the second case we compare the proposed method, applied on the digital holograms (2D test case), with a Discrete Fourier Filtering (DFF) that is based on the perfect knowledge of the signal bandwidth. In addition, a reality display of the results obtained on the digital holograms recorded in lensless configuration, and the comparison with the original noisy holograms, are realized and the details of the setup for 3D display is described.

4.1 Denoising method

Classic filter-based methods, as Fourier domain denoising [74] and wavelet domain denoising [9], have extensively been studied, but they can be applied only to some transform domains. Moreover, such denoising methods are greatly influenced by the change of signal parameters like frequency, amplitude, etc. Great effort has been spent on removing principally the speckle noise in digital holography [75] and speckle interferometry [76]. In order to effectively overcome the above-mentioned shortcomings of these denoising methods, it is relevant to design a reconstruction algorithms which are robust even in the presence of moderate or high-power noise level. The CS paradigm can be used as a denosing technique as demonstrate by BPDN or LARS method. The optimization problem, formulated for noisy data is given in Eq. (1.10) but it is based on the knowledge of the noise variance. This information not always is available and a previous estimation of the variance is necessary to obtain a good results using the aforementioned methods. Recently [96], an interesting and very simple procedure, based of an iterative noiseless recovery using the BP algorithm, has been proposed in order to suppress the zero-mean additive noise. Consider a signal $\tilde{\mathbf{x}}$ written as $\tilde{\mathbf{x}} = \bar{\mathbf{x}} + \mathbf{w}$, i.e. composed by a sum of an ideal noiseless signal $\bar{\mathbf{x}}$ and a zero-mean additive noise $\mathbf{w}$. Let $\mathbf{\Psi}$ the basis matrix such that $\mathbf{\Psi}\tilde{\mathbf{x}}$ is a sparse signal and let $\mathbf{\Phi}_i$, $i = 1, \ldots, K$ several $m \times n$

random sensing matrices. The denoising algorithm proposed in [96] consists of two steps:

- Compute $\hat{\mathbf{x}}_i$, $i = 1, \ldots, K$ as a solution of the noiseless recovery problem give in Eq. (1.10) using $\mathbf{\Phi}_i$

$$\hat{\mathbf{x}}_i \;=\; \arg\min \;\; \|\mathbf{\Psi x}\|_1 \quad \text{subject to} \;\; \mathbf{y}_i = \mathbf{\Phi}_i \mathbf{\Psi x} \tag{4.1}$$

  where $\mathbf{y}_i = \mathbf{\Phi}_i \mathbf{\Psi} \tilde{\mathbf{x}}$.

- The i-th recovered signal can be written as

$$\hat{\mathbf{x}}_i = \bar{\mathbf{x}} + \hat{\mathbf{w}}_i, \tag{4.2}$$

  where $\hat{\mathbf{w}}_i$ is a recovered noise. Therefore the denoised signal is given by

$$\mathbf{x}_{den} = \frac{1}{K} \sum_{i=1}^{K} \hat{\mathbf{x}}_i = \bar{\mathbf{x}} + \frac{1}{K} \sum_{i=1}^{K} \hat{\mathbf{w}}_i \tag{4.3}$$

  Is clear that, when $E\{\mathbf{w}\} = 0$, the term $\frac{1}{K} \sum_{i=1}^{K} \hat{\mathbf{w}}_i$ goes to zero when K increase.

Essentially, this algorithm simulates several acquisitions of a signal corrupted by zero-mean additive noise. Although this technique is very interesting, suffers from the problem that, to get a good denoising many simulations are needed, i.e. K must be very large. In addition, the recovered signal at each iteration, will be not exactly the signal given in Eq. (4.2), because the recovery problem (4.1) is optimal for the noiseless data. In other word, there will be a distortion of the denoised signal in Eq. (4.3) that is added to the approximation given by the finite dimension of K. To overcome these limitations, we have developed a new greedy algorithm [20] that produces an high efficient and robust denoising with a single noiseless recovery algorithm's execution, using a particular sensing matrix. In fact, simply placing $\mathbf{\Phi} = \mathbf{I}_n$ in the noiseless recovery method in Eq. (1.10), and solving it, is possible to obtain an accurate and robust denoising of a generic signal $\mathbf{x}$ corrupted by a zero-mean additive noise as well as a multiplicative noise. It is easy to show that the identity matrix satisfied the three conditions defined in the chapter 1, i.e. NSP, RIP and Coherence, and therefore it is a correct sensing matrix. Also note that it is a square matrix, i.e. $m = n$. This consequence of the choice is compatible with the fact that do not want to recover a signal with a few measurements but clean

up the signal from noise. Therefore, given a measurement $\tilde{\mathbf{x}}$, the denoising optimization problem is

$$\mathbf{v}_{den} = \arg\min \|\mathbf{v}\|_1 \quad \text{subject to} \quad \mathbf{\Psi}\tilde{\mathbf{x}} = \mathbf{v} \tag{4.4}$$

where $\mathbf{v}$ is a transform of the noisy signal, with $\mathbf{\Psi}$ chosen so that the transformed ideal noiseless signal is sparse. The algorithm that will be used to solve the denoising problem (4.4) is the StOMP algorithm using the solver "*SolveStOMP.m*", available online at website http://sparselab.stanford.edu/.

4.1.1 1D test case

Now consider an example of a sinusoidal signal $f(t) = \sin(20\pi t)$, with $t \in [0, 1]$, that is a sparse signal in the Fourier domain. It is corrupted by a zero-mean additive Gaussian noise $n(t)$ with standard deviation $\sigma = 0.2$. Both the method enveloped in [96], that we call Iterative Greedy Algorithm (IGA) and the method given in Eq. (4.4), called Identity Sensing Matrix Greedy Algorithm (ISMGA), are tested on the noisy signal. For the IGA we use 1000 iterations. Observing the Figure 4.1, is clear that both method give a good

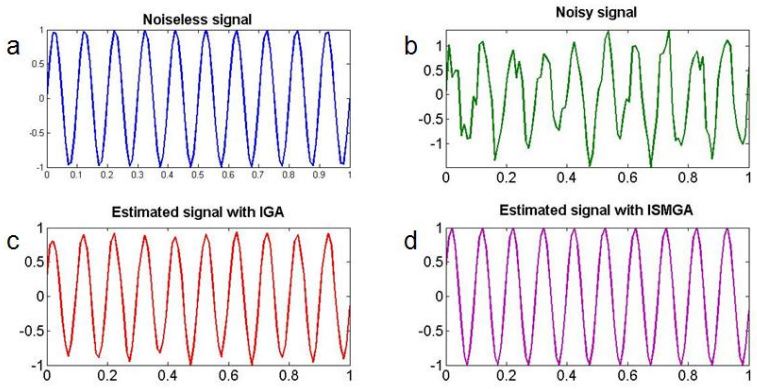

Figure 4.1: Results of the denoising algorithms for 1D example. (a) is the noiseless signal $f(t)$, (b) is the noisy signal corrupted by zero-mean additive Gaussian noise with standard deviation $\sigma = 0.2$. (c,d) are the recovered signals form IGA and ISMGA respectively.

results in terms of denoising, but the IGA is worse. This is caused by the two aforementioned limitations on the value of the number of iterations K

and the intrinsic distortion as a consequence by the application of the noiseless recovery algorithm on the noisy data. The ISMGA is obviously more efficient in terms of the computation time, because it is a one-shot execution, and it produces a small distortion then the method (4.1) because it considers all measurements through the identity sensing matrix. The final distortion is obtained by calculating mean squared error (MSE) between the noiseless sinusoidal signal $f(t)$ and the recovered ones, results $\text{MSE}_{\text{IGA}} = 0.1707$ and $\text{MSE}_{\text{ISMGA}} = 0.1437$.

4.2 2D case: denoising of digital holograms

Now we apply the ISMGA on the digital holograms considered in the sections 2.2.1 and 2.2.2. We solve the denoising optimization problem given in Eq. (4.4) replacing the measurement with $\tilde{\mathbf{h}}$ and the sparse transform with the Fresnel transform $\mathbf{F}_\delta$. The problem optimization becomes

$$\mathbf{v}_{den} = \arg\min \ \|\mathbf{v}\|_1 \quad \text{subject to} \quad \mathbf{F}_\delta \tilde{\mathbf{h}} = \mathbf{v} \tag{4.5}$$

As has been shown in the chapter 3, the distance of reconstruction δ is different for the examples considered. In fact, because the numerical reconstruction of digital holograms recorded in microscope configuration has the higher degree of sparsity in the BFP, for this kind of holograms we set $\delta = d_{BFP}$, while for digital holograms recorded in lensless configuration the best choice is the plane of focus, i.e. for the astronaut $\delta = d$ and for Venus $\delta = \frac{r-d}{rd}$. This last setting is related to the fact that the digital hologram of Venus was recorded using a spherical reference wave of curvature r.

4.2.1 BFP reconstruction optimization

Consider again the digital holograms recorded in microscope configuration shown in section (2.2.1). We apply the ISMGA for both digital hologram of the object (MEMS and in-vitro cell) and its reference hologram. The results of the denoising algorithm are show in Figure 4.2 and Figure 4.3

Is important to note that, it seems that some areas of noise in the BFP reconstruction of in-vitro cell have not been suppressed by the algorithm but it is a false sense. In fact these areas that seems noise are the residual zero-order that high-pass kernel is not able to remove, so it's part of the useful signal for the algorithm. The denoised holograms are obtained by the back propagation, of the denoised complex field, in the hologram plane, using Eq. (2.22) with

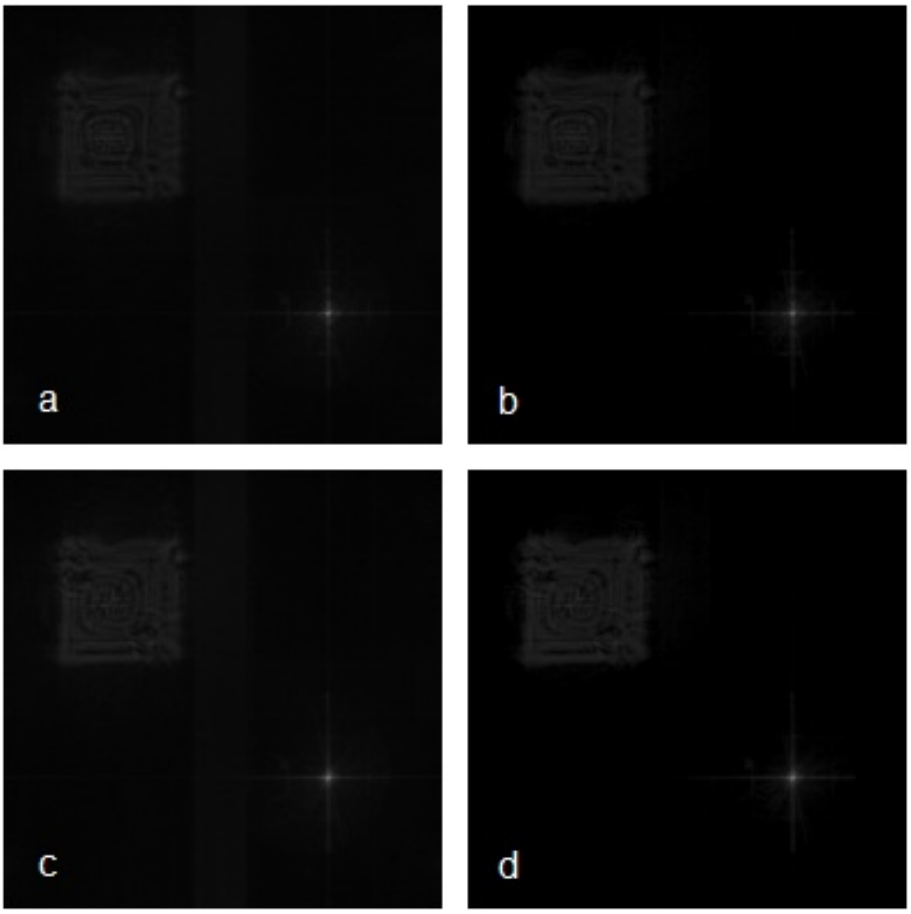

Figure 4.2: Results of the ISMGA denoising (b,d) on the holograms of MEMS (a,c)

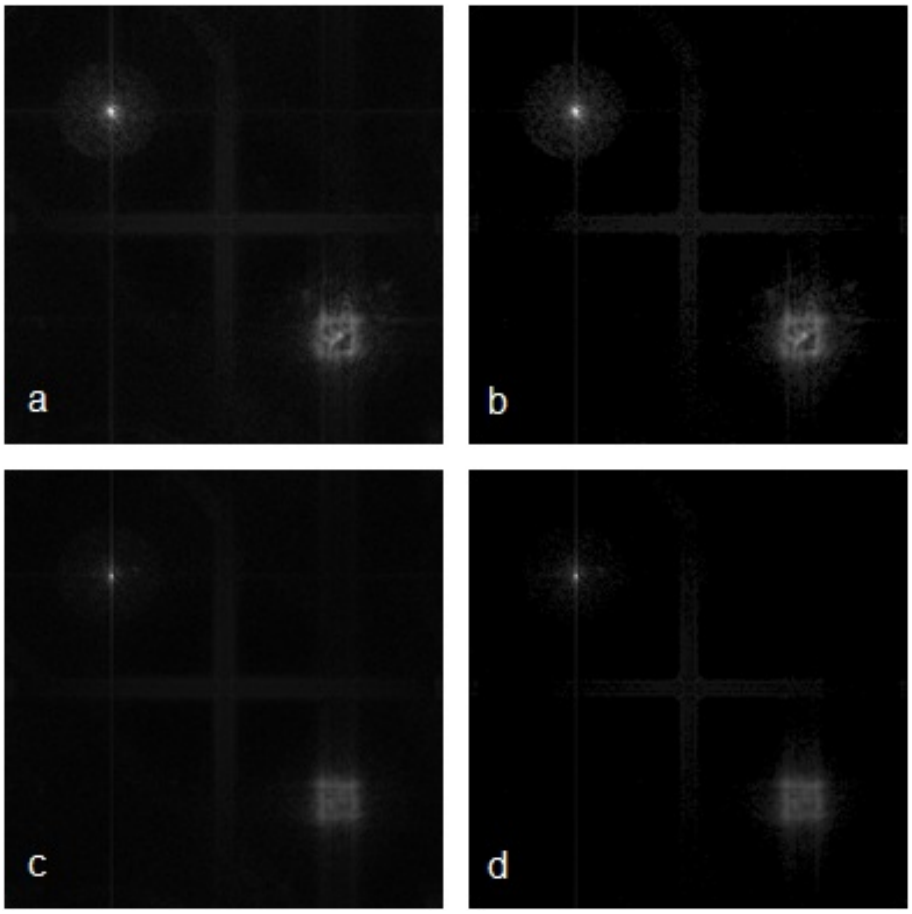

Figure 4.3: Results of the ISMGA denoising (b,d) on the holograms of in-vitro cell (a,c)

$d = d_{BFP}$ and pixels pitch according to the Eq. (2.23). Finally the numerical reconstructions at the in-focus distance is computed. The comparison between the original in-focus reconstructions and the denoised ones are given for one of the holograms for both MEMS and in-vitro cell and are showed in Figure 4.4

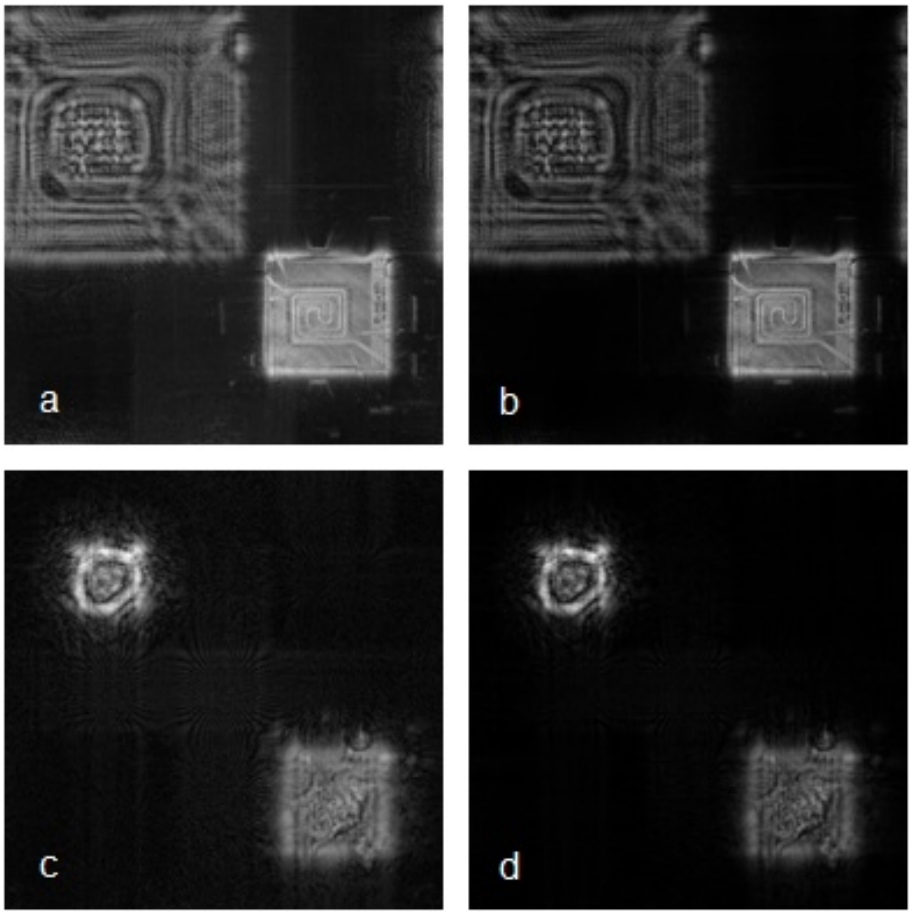

Figure 4.4: Results of the ISMGA denoising (b,d) on the holograms of MEMS (a) and in-vitro cell (b) in the in-focus plane

Finally, we consider again the computation of phase maps, as previous show (section 2.4.3). As show in Figure 2.13 (a), the unwrapping process applied on the phase reconstruction of MEMS was not able to remove all of phase jumps. Instead, computing the phase map with the denoised holograms of

MEMS, the phase jumps are eliminated. This means that, the ISMGA helped the unwrapping procedure, as shown the Figure 4.5.

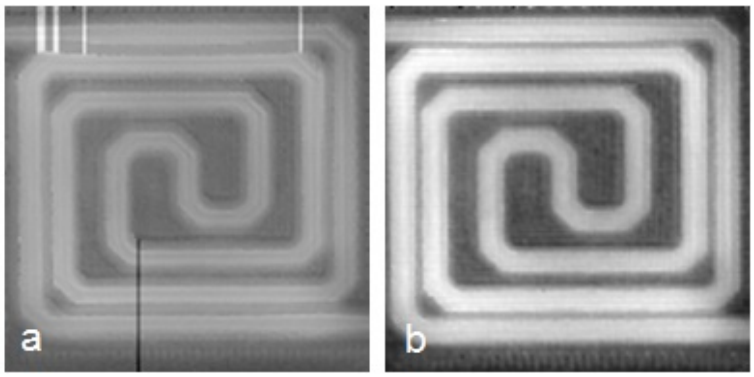

Figure 4.5: Unwrapped phase of MEMS without denoising (a) and after ISMGA denoising (b)

4.2.2 Fresnel reconstruction optimization

For digital holograms recorded in lensless configuration, consider the ISMGA in which the in-focus distance for the +1 order is placed. The results of the denoising algorithm are shown in Figure 4.6 for the astronaut puppet and Figure 4.7 for the Venus statuette.

Also in this case, the denoised images present the residual of zero-order suppression.

4.3 3D holographic display

The numerical reconstruction of holograms recorded in lensless configuration can be either performed numerically for a 2D screen or for display in 3D by a spatial light modulator (SLM) [97], [98], [99]. Since the hologram can be numerically transformed [100] to change the distance at which it will appear in focus in the reconstruction process, an observer will see a 3D scene in both numerical and optical reconstructions, the last one using a SLM device [57].

Figure 4.8 describes the set-up used for the optical projection of the 3D scene. We use a DPSS laser emitting at $\lambda = 532nm$. The laser beam is expanded in such a way as to obtain a convergent beam that impinges on the

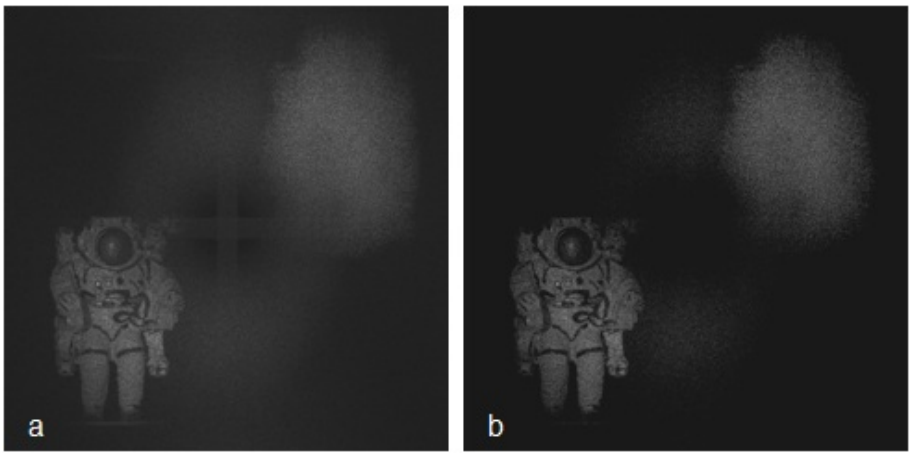

Figure 4.6: Original numerical reconstruction of the astronaut (a) and denoised one(b)

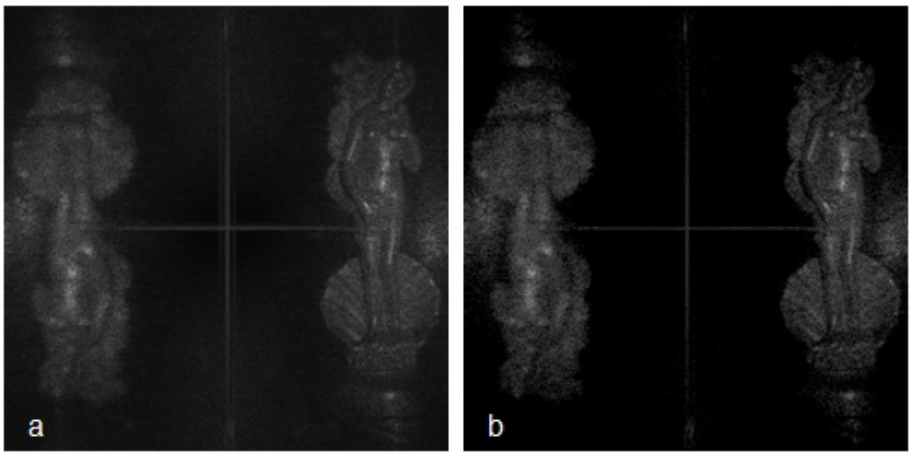

Figure 4.7: Original numerical reconstruction of Venus (a) and denoised one(b)

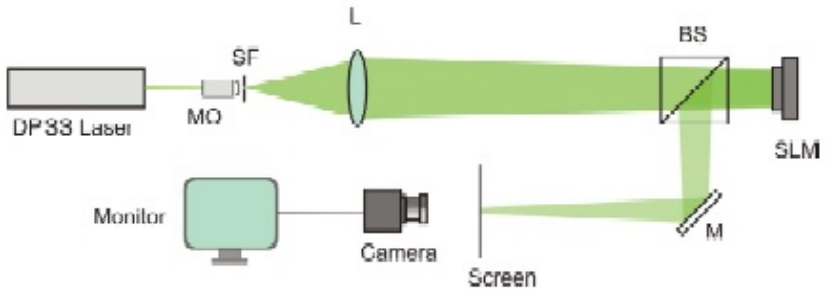

Figure 4.8: Set-up used for the optical projection of the 3D scene; MO: microscope objective, SF: spatial filter, L: lens, BS: beam splitter, SLM: spatial light modulator, M: mirror.

SLM-LCOS (PLUTO-by Holoeye, $8\mu m$ pixel pitch) that displays the hologram. The real images are projected onto a scattering screen at a certain distance $\tilde{d}$ from the SLM and, then, acquired by a camera. The distance in which the projection goes in-focus can be different with respect the numerical in-focus distance because the physical parameters of SLM (like pixel pitch or wavelength) differ, in general, from the recording parameters. However it is possible to compute exactly the distance $\tilde{d}$ as a function of these changes [57]. The aim of this section is to demonstrate that the ISMGA produces an improvement of the quality of the display as well as of the numerical reconstructions shown in section 4.2.2. Therefore the original recorded holograms of astronaut and Venus and the denoised ones, obtained simply by $\mathbf{h}_{den} = \mathbf{F}_{\delta}^{-1}\mathbf{v}_{den}$, i.e. the back propagation of the denoised complex field in the hologram plane, are posed as input of SLM and the in-focus projections are acquired. The recorded projections are showed in Figure 4.9

The projected holograms shows that the ISMGA denoising increases the quality also of the optical reconstruction. In fact, in this case, the concept of quality is related to the amount of laser light that reconstructs the object. A quantitative analysis about the effectiveness of the ISMGA denoising for both numerical and optical reconstructions is give in the following section.

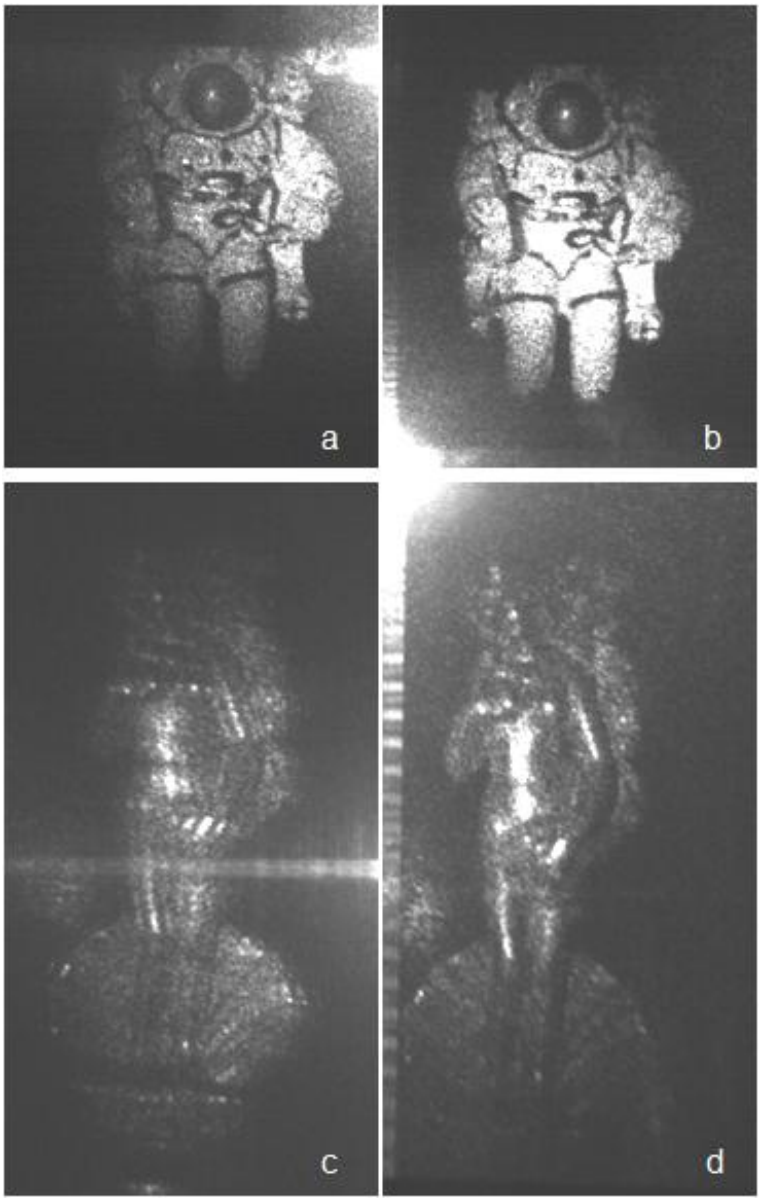

Figure 4.9: Projections of lensless holograms using SLM. (a) and (c) are the magnification of the +1 order projections of the original holograms, while (b) and (d) are the projections of the denoised ones.

4.4 Analysis of results

In order to quantify the benefits introduced by the ISMGA denoising, two different parameters of efficiency are defined:

- The signal to distortion ratio (SDR) defined as

$$\text{SDR} = \frac{\left\|\widetilde{\mathbf{I}}\right\|_2}{\left\|\widetilde{\mathbf{I}} - \widehat{\mathbf{I}}\right\|_2} \tag{4.6}$$

  where $\|\cdot\|_2$ is the ℓ_2-norm, $\widetilde{\mathbf{I}} = \left|\mathbf{F}_d\tilde{\mathbf{h}}\right|$ is the amplitude of the original in-focus digital reconstruction and $\widehat{\mathbf{I}} = \left|\mathrm{F}_d\hat{\mathbf{h}}\right|$ is the processed one.

- The measure of contrast given by Eq. (2.27), where $\mathbf{I}$ in one case is the amplitude in-focus digital reconstruction of original hologram and in the other cases is the amplitude of the processed one.

The ISMGA denoising is compared with the classical DFF [74], that is a well known denoising technique. For digital holograms, this method consists into numerically compute the propagation from the discrete hologram plane to the discrete Fourier planed. Then, the Fourier plane data are filtered and inverse discrete Fourier transformed to the image plane.

Table 4.1 and Table 4.2 report the computation of the two parameters of efficiency for the cases under analysis. In particular, for MEMS and in-vitro cell, it consider only one of the two cases for each one.

	DFF	**ISMGA**
Astronaut	1.1171	2.3691
Venus	1.1126	4.6181
MEMS	1.0172	3.8394
Cell	1.2427	6.2163

Table 4.1: Calculation of SDR

These results show that the ISMGA denoising provides gains both in terms of SDR and image contrast C and this shows its effective efficiency and robustness. Finally, in order to evaluate the improvement of projections in the display test, we compute the percentage increase of intensity, G, for the recorded projections reported in Figure 4.9

	Noisy hologram	**DFF**	**ISMGA**
Astronaut	1.2581	1.8694	2.5757
Venus	1.4489	2.2017	4.8880
MEMS	1.0389	1.6584	2.1905
Cell	1.8801	2.8024	3.1676

Table 4.2: Calculation of contrast C

$$G = \frac{\sum_{(x,y)\in SR}\left(\widehat{\mathrm{I}} - \widetilde{\mathrm{I}}\right)}{\sum_{(x,y)\in SR}\widetilde{\mathrm{I}}} \tag{4.7}$$

where SR means signal regions, i.e. only the +1 order. For the puppet of astronaut we have $G \approx 31\%$, while for the statuette of Venus results $G \approx 16\%$, then provides the improvement also in the display step.

Conclusions

In this thesis, the CS framework has been considered as a new methodology of signals recovery. In particular, has been described how to recover a signal that admits a sparse representation in a suitable transform domain from undersampled measurements, and how to overcome the limit imposed by the sampling theorem for this class of signals. We are focused on the property of sparsity for the signals, the design of the sensing matrices for different applications and the description of the problem of signal recovery in both cases of noiseless signals and noisy signals. Several algorithms have been considered in order to solve the recovery problem as BP, OMP, StOMP and LARS method. CS has attracted considerable attention in areas of applied mathematics, computer science, electrical engineering and other research fields because it is possible to represent many natural signals using only a few non-zero coefficients in a suitable basis. The thesis has mainly addressed the issue regarding the application of CS in the field of DH, that is a relatively recent interferometric technique that has permitted many spectacular applications such as microscopic imaging by phase-contrast digital holographic microscopy, 3D object recognition and 3D dynamic display. The full holographic process has been mathematically treated, from the digital recording to the numerical reconstruction, considering the two largest classes of digital holograms, those acquired in the microscope configuration and those acquired in lensless configuration. For both classes, we have discussed about the numerical reconstruction, obtained by the discrete version of the Fresnel integral, in order to highlight the physical properties of the three diffraction orders. The analysis of these diffracted complex fields is achieved through the in-focus numerical reconstructions for both kind of digital holograms and also the BFP reconstructions for the class of digital holograms recorded in microscope configuration. For this purpose, an algorithm of automatic search of the in-focus reconstruction distance and BFP distance has been described. Obviously, in order to apply the CS framework on digital holograms, we have studied the properties of the sparsity of the digital

holograms. Previous studies have already shown how to combine the off-axis frequency-shifting DH to perform quadrature-resolved random measurements of an optical field in a diffraction plane and a sparsity minimization algorithm to reconstruct the image. The sparsity of digital holograms is obtained by calculating the gradient of the in-focus numerical reconstruction. Moreover, this CS-based imaging scheme has the limitation that it can be applied only to digital holograms recorded in microscope configuration. In fact, it is shown that the gradient of the in-focus numerical reconstruction in the case of holograms acquired in lensless configuration is not a sparse image. An important contribution of this thesis is to propose a unified scheme for the recovery of digital holograms belonging to both the aforementioned classes, based on the sparsity property of the in-focus numerical reconstruction for the lensless case and of the BFP reconstruction for the microscope case. Two examples for each class of holograms have been considered and the BP algorithm has been applied for the recovery from undersampled measurements. The results show that the Fresnel transform, parameterized in terms of the reconstruction distance, is a suitable and general sparse domain for digital holograms. However, since digital holograms are real signals, and then corrupted by noise, it is also considered the problem of recovery for noisy signals. In this case, the recovery algorithms, typically used, are BPDN and the modified LARS. In both cases is necessary the knowledge about the statistics of noise, but this information is not always available. The principal contribution of the thesis is to design and implement a new greedy algorithm that does not use any a priori information about the statistics of the noise. This algorithm can be obtained by the recovery problem for noiseless signals simply replacing an identity sensing matrix. In fact, using the total information contained in the recorded digital holograms, we are able to estimate the support of the useful signal suppressing the noise components. Also in this case, the sparsity domain considered is the Fresnel transform of the digital holograms in the in-focus plane and BFP. The proposed method, called ISMGA, is compared with another greedy algorithm, based on repeated BP recovery with different random sensing matrices, and the classic filtering in Fourier domain, which is based on the perfect knowledge of the signal bandwidth. The results show that the algorithm is better than the other two, in terms of two parameters of efficiency, SDR and image contrast, demonstrating its robustness and its effectiveness. In addition, for the digital holograms recorded in lensless configuration, we have shown that the ISMGA denoising also produces improvements in the 3D display. We have made the projection experiments, using the SLM, and quantified the percentage increase of image

contrast for the originally recorded digital holograms and the processed one with the ISMGA denoising. For both examples considered, we get a significant increase in the image contrast, 31% in one case and 16% in the other one. Ultimately the thesis work has contributed to the optimization of the processes of digital recording, numerical reconstruction and 3D display thanks the CS framework, which will surely be developed in other fields of research based on the signal processing.

Appendix A

Appendix

A.1 Review of Convex Optimization

In this appendix there are a description of a special class of optimization problems called *convex optimization*. These particular problems can be to solve "efficiently", in the sense that we can solve many real-world problems in a reasonable amount of time. In other words, it means that, theoretically, we can solve problems in time that depends only polynomially on the problem size. In the following subsections there are a formulation of a general Convex Optimization Problem (COP), some special cases of problems and different example of nonconvex problems that can be transformed in a convex problems. Most of the material reported in this appendix is heavily based on the book Convex Optimization [101] by Boyd and Vandenberghe (available for free online).

A.1.1 Formulation of COP

A mathematical optimization problem has the form

$$\min_{\mathbf{x}} \quad f(\mathbf{x}) \quad \text{subject to} \quad \mathbf{x} \in C \tag{A.1}$$

where $\mathbf{x}$ is a n-vector called optimization variable of the problem, $f : R^n \rightarrow R$ is the objective function and $\mathbf{x} \in C$ is the constraint function. The problem (A.1) is a COP if C is a convex set and f is a convex function of $\mathbf{x}$. For the convex set, the condition is:

Definition A.1 *A set C is convex if, for any $\mathbf{x}, \mathbf{y} \in C$ and $\theta \in (0, 1)$*

$$\theta\mathbf{x} + (1 - \theta)\mathbf{y} \in C$$

In the Figure A.1 there is an example of both convex and non-convex sets. Instead for the objective function we have:

Definition A.2 *Let $\mathcal{D}(f)$ the domain of $f : R^n \rightarrow R$. The function f is convex if $\mathcal{D}(f)$ is a convex set and if, for all $\mathbf{x}, \mathbf{y} \in \mathcal{D}(f)$ and $\theta \in (0, 1)$*

$$f(\theta\mathbf{x} + (1 - \theta)\mathbf{y}) \leq \theta f(\mathbf{x}) + (1 - \theta)f(\mathbf{y})$$

In the Figure A.2 there is an example of convex function.

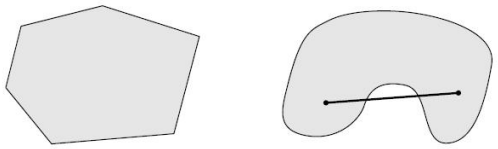

Figure A.1: Examples of a convex set (left) and a non-convex set (right)

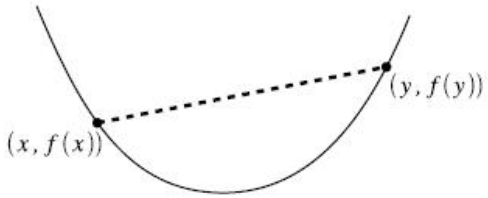

Figure A.2: Graph of a convex function. The line connecting two points on the graph must lie above the function.

Typically, the convex set C is represented by the inequality constraint functions and equality constraint functions. In this case, the convex optimization problem (A.1) becomes

$$\min_{\mathbf{x}} \ f(\mathbf{x}) \ \text{ subject to } \ \begin{cases} g_i(\mathbf{x}) \leq 0 & i = 1, \ldots, p \\ h_k(\mathbf{x}) = 0 & k = 1, \ldots, q \end{cases} \tag{A.2}$$

where g_i, for $i = 1, \ldots, p$, are a convex functions and h_k, for $k = 1, \ldots, q$ are affine functions. Finally, the optimal value of an optimization problem is denoted $\mathbf{x}^*$ and is equal to the minimum argument value of the objective function in the feasible region, identified by the both inequality and equality constraints.

$$\mathbf{x}^* = \arg\min \; f(\mathbf{x}) \;\; \text{subject to} \;\; \begin{cases} g_i(\mathbf{x}) \leq 0 & i = 1, \ldots, p \\ h_k(\mathbf{x}) = 0 & k = 1, \ldots, q \end{cases} \tag{A.3}$$

A.1.2 Special cases of COP

Now it consider several classes of convex optimization problems, based on the forms that can take both the objective function and the constraints. Because the following problems can be solved in a polynomial computational time, often tries to formulate an optimization problem in one of these forms.

- **Linear Programming:** a convex optimization problem is a linear program (LP) if both the objective function f and inequality constraints g_i are affine functions. In other words, these problems have the form

$$\min_{\mathbf{x}} \;\; \mathbf{c}^T\mathbf{x} + d \;\; \text{subject to} \;\; \begin{cases} \mathbf{G}\mathbf{x} \preceq \mathbf{h} \\ \mathbf{A}\mathbf{x} = \mathbf{b} \end{cases} \tag{A.4}$$

  where $\mathbf{c} \in R^n$, $d \in R$, $\mathbf{G} \in R^{m \times n}$, $\mathbf{h} \in R^m$, $\mathbf{A} \in R^{l \times n}$ and $\mathbf{b} \in R^l$ are defined by the problem, and the symbol "$\preceq$" denotes elementwise inequality.

- **Quadratic Programming:** a convex optimization problem is a quadratic program (QP) if the inequality constraints g_i are still all affine, but if the objective function f is a convex quadratic function. Therefore, these problems have the form

$$\min_{\mathbf{x}} \;\; \frac{1}{2}\mathbf{x}^T\mathbf{P}\mathbf{x} + \mathbf{c}^T\mathbf{x} + d \;\; \text{subject to} \;\; \begin{cases} \mathbf{G}\mathbf{x} \preceq \mathbf{h} \\ \mathbf{A}\mathbf{x} = \mathbf{b} \end{cases} \tag{A.5}$$

  where $\mathbf{P}$ is a symmetric positive semidefinite matrix, i.e. $\mathbf{P} \in \mathcal{S}_+^n$.

- **Semidefinite Programming:** this last example is different than the previous one because the optimization variable of the problem is a $n \times n$ matrix. This class of problems is becoming more prevalent in many areas

of research. We say that a convex optimization problem is a semidefinite program (SDP) if it is of the form

$$\min_{\mathbf{X}} \ \mathrm{tr}\,(\mathbf{PX}) \quad \text{subject to} \quad \begin{cases} \mathrm{tr}\,(\mathbf{A}_i\mathbf{X}) = b_i \quad i = 1, \ldots, p \\ \mathbf{X} \succeq 0 \end{cases} \tag{A.6}$$

where the symmetric matrices $\mathbf{P}, \mathbf{A}_1, \ldots, \mathbf{A}_p$ are defined by the problem, and the constraint $\mathbf{X} \succeq 0$ means that $\mathbf{X}$ must to be positive semidefinite.

However, there are other known forms of convex optimization problems, such as Geometric Programming, and special cases in which there are a particular functions in the formulation of problems as quasiconvex functions or log-convex functions. In these latter cases it is always possible to bring to a convex optimization problem using a suitable change of optimization variable. However, there are many cases where it is not possible to formulate the problem in a convex or quasiconvex program. The next section analyzes this situation, providing a solution to the issue.

A.1.3 Nonconvex optimization problems

In the section A.1.1, it was said that the optimization problem (A.2) is convex if the objective function and the inequality constraint functions are convex, and the equality constraint functions are affine. Therefore, a problem is a nonconvex optimization problem if if one of these conditions are not met. In this case it is possible to rewrite the nonconvex optimization problem in a convex form using the *relaxation method*. In relaxation, each nonconvex constraint (i.e. the objective function) is replaced with a looser, but convex, constraint (i.e. the objective function) and provides a lower bound on the optimal value of the nonconvex problem. For example, we have applied this technique to the optimization problem (1.7) obtaining the convex optimization problem (1.8). Finally, in some situations, it is possible to have that the lower bound of optimal value of relaxed problems is equal to the optimal solution of nonconvex problem.

A.2 MATLAB code's description

In this appendix are reported the list of scripts, realized in MATLAB, for the analysis considered in this thesis. The scripts are related to the chapter in which

they are used. We give only a list of routines used with a simple explanations, without providing the MATLAB codes.

A.2.1 Scripts for chapter 1

The chapter 1 describes the mathematical formulation of the CS framework and the there aren't any simulations. However describes the algorithms that are used to solve the recovery problem for both noiseless and noisy signals. The following list contains the MATLAB scrips used for the recovery problem that are available on the website http://sparselab.stanford.edu/, as is mentioned several times in the text of the thesis.

- **SolveBP.m**

  function *sol* = SolveBP(*A, y, N, maxIters, lambda, OptTol*)
  SolveBP: Solves a Basis Pursuit problem
  Usage
  sol = SolveBP(*A, y, N, maxIters, lambda, OptTol*)
  Input
  A: either an explicit $n \times N$ matrix, with rank$(A) = \min(N, n)$ by assumption, or a string containing the name of a function implementing an implicit matrix (see below for details on the format of the function).
  y: a vector of length n.
  N: length of solution vector.
  maxIters: maximum number of PDCO iterations to perform, default 20.
  lambda: if 0 or omitted, Basis Pursuit is applied to the data, otherwise, Basis Pursuit Denoising is applied with parameter lambda (default 0).
  OptTol: error tolerance, default 1e-3.
  Outputs
  sol: solution of BP
  Description
  SolveBP solves the basis pursuit problem by reducing it to a linear program, and calling PDCO, a primal-dual log-barrier algorithm. Alternatively, if lambda differ to 0, it solves the Basis Pursuit Denoising (BPDN) problem by transforming it to an SOCP, and calling PDCO. The matrix *A* can be either an explicit matrix, or an implicit operator implemented as a function.

- **SolveStOMP.m**

function [*sol, numIters*] = SolveStOMP(*A, y, N, thresh, param, maxIters, verbose, OptTol*)
SolveStOMP: Implementation of Iterative Threshold-Selective Projection algorithm
Usage
[*sol, numIters*] = SolveStOMP(*A, y, N, thresh, param, maxIters, verbose, OptTol*)
Input
A: Either an explicit $n \times N$ matrix, with rank$(A) = \min(N, n)$ by assumption, or a string containing the name of a function implementing an implicit matrix (see below for details on the format of the function).
y: a vector of length n.
N: length of solution vector.
thresh: thresholding strategy: FDR or FAR. default is FDR.
param: sensitivity parameter for threshold selection.
maxIters: maximum number of StOMP iterations to perform, default 10.
verbose: 1 to print out detailed progress at each iteration, 0 for no output (default).
OptTol: error tolerance, default 1e-5.
Outputs
sol: solution of StOMP.
numIters: total number of steps taken.
Description
SolveStOMP implements the Stagewise Ortogonal Matching Pursuit, as described in the paper [37].

- **MatrixEnsemble.m**

  function *Phi* = MatrixEnsemble(*n,m,ensemble*)
  MatrixEnsemble: Generates a random matrix of size *n* by *m*.
  Usage
  Phi = MatrixEnsemble(*n,m,ensemble*)
  Inputs
  n: number of rows.
  m: number of columns.
  ensemble: string containing name of matrix ensemble: ”USE”, ”RSE”, ”Fourier”, ”RST”, ”Hadamard”, ”URP”, ”IR”. Default is ’USE’.
  Outputs
  Phi: *n* by *m* matrix from the specified ensemble.
  Description

This function creates a matrix from the specified random matrix ensemble. The following random ensembles are implemented:
"USE" - Uniform spherical ensemble. Columns are *n*-vectors, uniformly distributed on the sphere S^{n-1} (default).
"RSE" - Random signs ensemble. Entries in the matrix are chosen from a Bernoulli $+/-1$ distribution, and columns are normalized to have unit Euclidean length.
"Fourier" - Partial Fourier ensemble. Matrices in this ensemble are generated by taking the *m* by *m* Fourier matrix, sampling *n* rows at random, and scaling columns to have unit Euclidean length.
"RST" - Partial RST (Real Fourier) ensemble. See 'Fourier' above.
"Hadamard" - Partial Hadamard ensemble. Matrices in this ensemble are generated by taking the m by m Hadamard matrix, sampling *n* rows at random, and scaling columns to have unit Euclidean length.
"URP" - Uniform Random Projection ensemble. Matrices in this ensemble are generated by sampling *n* rows of an *m* by *m* random orthogonal matrix.
"IR" - Identity and Random ortho-basis. An *n* by *2n* matrix is constructed, as the concatenation of the *n* by *n* identity and an *n* by *n* random ortho-basis.

A.2.2 Scripts for chapter 2

The chapter 2 describes the full holographic process, from the recorded hologram to the image formation. Therefore we give three routines related to the numerical reconstruction of the digital holograms, the back propagation of the numerical reconstruction in the hologram plane and finally the auto-focusing algorithm.

- **RecoHolo.m**

  function *NR* = RecoHolo(*H,d*)
  RicoHolo: compute the numerical reconstruction of an hologram.
  Usage
  NR = RecoHolo(*H,d*)
  Inputs
  H: recorded hologram.
  d: reconstruction distance (mm).
  Output
  NR: numerical reconstruction of the hologram at distance *d*.

Description
This function implement the discrete version of Fresnel transform given in Eq. (2.22).

- **BackProp.m**

  function H = BackProp(NR,d)
  BackProp: compute the back propagation of the reconstructed complex field in the hologram plane.
  Usage
  H = BackProp(NR,d)
  Inputs
  NR: numerical reconstruction of the recorded hologram at distance d, obtained using "RecoHolo.m".
  d: reconstruction distance (mm).
  Output
  H: digital hologram.
  Description
  This function implement the discrete version of Fresnel transform given in Eq. (2.22) using the distance $-d$ and the pixel pitches given in Eq. (2.23).

- **Autofocus.m**

  function [NRf,df] = Autofocus(H,$dmin$,$dmax$,$iter$)
  Autofocus: compute the in-focus distance for the +1 order when the input is an hologram recorded in lensless configuration; compute the BFP distance for the +1 order when the input is an hologram recorded in microscope configuration.
  Usage
  [NRf,df] = Autofocus(H,$dmin$,$dmax$,$iter$)
  Inputs
  H: recorded hologram.
  $dmin$: lower bound of the searching interval.
  $dmax$: upper bound of the searching interval.
  $iter$: number of iterations.
  Outputs
  NRf: numerical reconstruction of the hologram at estimated distance.
  df: estimated distance: in-focus plane for digital holograms recorded

in lensless configuration, BFP for digital holograms recorded in microscope configuration.
Description
This function implement the algorithm given in [86]. It define a grid of research considering *N=iter* equally spaced points in the range [*dmin,dmax*]. At each point *di*, it compute the numerical reconstruction of the hologram using "RecoHolo.m" and its Tamura coefficient, given in Eq. (2.27). At the end, evaluate the maximum value of the *N* realization of the Tamuta coefficient which corresponds to the output *df*. Finally, compute the output *NRf* as a numerical reconstruction of the hologram at distance *df* using "RecoHolo.m".

A.2.3 Scripts for chapters 3 and 4

In these two chapters there is the description of the CS theory applied in DH. More precisely, the chapter 3 describes the methodology used for the recovery of the digital holograms from undersampled measurements, while the chapter 4 addresses the problem of denoising. In both cases, we use all the routines described above, therefore we give the step-by-step descriptions of the scripts for recovery and denoising, which are listed below.

- **RecoveryBP.m**

  function [*RecHOLO,RecPSIh*] = RecoveryBP(*H,d,m*)
  RecoveryBP: compute the recovered hologram form undersampled measurements using BP.
  Usage
  [*RecHOLO,RecPSIh*] = RecoveryBP(*H,d,m*)
  Inputs
  H: recorded hologram.
  d: reconstruction distance (mm).
  m: number of samples in the sensing matrix **Output**
  RecHOLO: recovered hologram.
  RecPSIh: recovered numerical reconstruction.
  Description
  This function permits to obtain the recovery of a digital hologram from undersampled measurements. The steps of the algorithm are:

  1. Numerical reconstruction of the hologram at distance *d*: *NR* = RecoHolo(*H,d*).

2. Vectorization of the numerical reconstruction: *nr*=vec(*NR*).
3. Compute the sensing matrix: *PHI* = MatrixEnsemble(*m,N,'USE'*), where *N* is the length of the vector *nr*.
4. Compute the measurements: *y*=*PHInr*.
5. Solve the Basis Pursuit problem: *sol* = SolveBP(*PHI,y,N*).
6. Compute the outputs: *RecPSIh*=reshape(*sol*), *RecHOLO* = BackProp(*RecPSIh,d*).

- **ISMGA.m**

  function [*HOLOden,RECden*]=ISMGA(*H,d*)
  ISMGA: compute the denoised hologram using the identity sensing matrix in the StOMP.
  Usage
  [*HOLOden,RECden*]=ISMGA(*H,d*)
  Inputs
  H: recorded hologram.
  d: reconstruction distance (mm).
  Output
  HOLOden: denoised hologram.
  RECden: denoised numerical reconstruction.
  Description
  This function permits to obtain the denoising of a digital hologram using the ISMGA described in the chapter 4. The steps of the algorithm are:

  1. Numerical reconstruction of the hologram at distance *d*: *NR* = RecoHolo(*H,d*).
  2. Vectorization of the numerical reconstruction: *nr*=vec(*NR*).
  3. Compute the sensing matrix: $PHI = \mathbf{I}_N$, where *N* is the length of the vector *nr*.
  4. Solve the Stagewise Orthogonal Matching Pursuit problem: [*sol, numIters*] = SolveStOMP(*PHI,nr,N*).
  5. Compute the outputs: *RECden*=reshape(*sol*), *HOLOden* = BackProp(*RECden,d*).

Bibliography

[1] E.J. Candes and T. Tao. Near-optimal signal recovery from random projections: Universal encoding strategies? *IEEE Trans. Inform. Theory*, 52(12):5406–5425, 2006.

[2] D.L. Donoho. Compressed sensing. *IEEE Trans. Inform. Theory*, 52(4):1289–1306, 2006.

[3] E.J. Candes. Compressive sampling. *In Proc. Int. Congress of Math.*, 2006.

[4] E.J. Candes and J. Romberg. Quantitative robust uncertainty principles and optimally sparse decompositions. *Found. Comput. Math.*, 6(2):227–254, 2006.

[5] E.J. Candes, J. Romberg, and T. Tao. Robust uncertainty principles: Exact signal reconstruction from highly incomplete frequency information. *IEEE Trans. Inform. Theory*, 52(2):489–509, 2006.

[6] E.J. Candes, J. Romberg, and T. Tao. Stable signal recovery from incomplete and inaccurate measurements. *Comm. Pure Appl. Math.*, 59(8):1207–1223, 2006.

[7] J. Tropp and S. Wright. Computational methods for sparse solution of linear inverse problems. *Proc. IEEE*, 98(6):948–958, 2010.

[8] D. Taubman and M. Marcellin. *JPEG 2000: Image Compression Fundamentals, Stan- dards and Practice*. Kluwer, 2001.

[9] D. Donoho. Denoising by soft-thresholding. *IEEE Trans. Inform. Theory*, 41(3):613–627, 1995.

[10] V. Vapnik. *The Nature of Statistical Learning Theory*. Springer-Verlag, 1999.

[11] R. Tibshirani. Regression shrinkage and selection via the lasso. *J. Royal Statist. Soc B*, 58(1):267–288, 1996.

[12] B. Olshausen and D. Field. Emergence of simple-cell receptive

eld properties by learning a sparse representation. *Nature*, 381:607–609, 1996.

[13] S. Mallat. *A Wavelet Tour of Signal Processing*. Academic Press, 1999.

[14] A.M. Tulino, G. Caire, S. Shamai, , and S. Verdú. Support recovery with sparsely sampled free random matrices. *The IEEE International Symposium on Information Theory (ISIT 2011)*, 2011.

[15] J.W. Goodman and R.W. Lawrence. Digital image formation from electronically detected holograms. *Appl. Phys. Lett*, 11(3):77–79, 1967.

[16] M.A. Kronrod, N.S. Merzlyakov, and L.P. Yaroslavskii. Reconstruction of a hologram with a computer. *Sov. Phys. Tech. Phys*, 17:333–334, 1972.

[17] U. Schnars and W. Juptner. Direct recording of holograms by a ccd target and numerical reconstruction. *Appl. Opt.*, 33:179–181, 1994.

[18] M.M. Marim, M. Atlan, E. Angelini, , and J-C Olivo-Marin. Compressed sensing with off-axis frequency-shifting holography. *Opt. Lett.*, 35:871–873, 2010.

[19] M.M. Marim, E. Angelini, J-C Olivo-Marin, , and M. Atlan. Off-axis compressed holographic microscopy in low-light conditions. *Opt. Lett.*, 36:79–81, 2011.

[20] P. Memmolo, I. Esnaola, A. Finizio, M. Paturzo, P. Ferraro, and A.M. Tulino. Universal denoising in digital holography using compressed sensing. *in revision*, 2011.

[21] H. Nyquist. Certain topics in telegraph transmission theory. *Trans. AIEE*, 47:617–644, 1928.

[22] C. Shannon. Communication in the presence of noise. *Proc. Institute of Radio Engi- neers*, 37(1):10–21, 1949.

[23] A.M. Bruckstein, D.L. Donoho, and M. Elad. From sparse solutions of systems of equations to sparse modeling of signals and images. *SIAM Rev.*, 51(1):34–81, 2009.

[24] M. Elad. *Sparse and Redundant Representations: From Theory to Applications in Signal and Image Processing*. Springer, 2010.

[25] R. DeVore. Nonlinear approximation. *Acta Numerica*, 7:51–150, 1998.

[26] T. Hastie, R. Tibshirani, and J. Friedman. *The Elements of Statistical Learning*. Springer, 2001.

[27] E.J. Candes and T. Tao. Decoding by linear programming. *IEEE Trans. Inform. Theory*, 51(12):4203–4215, 2005.

[28] D. Donoho and M. Elad. Optimally sparse representation in general (nonorthogonal) dictionaries via l_1 minimization. *Proc. Natl. Acad. Sci.*, 100(5):2197–2202, 2003.

[29] J. Tropp and A. Gilbert. Signal recovery from partial information via orthogonal matching pursuit. *IEEE Trans. Inform. Theory*, 53(12):4655–4666, 2007.

[30] L. Welch. Lower bounds on the maximum cross correlation of signals. *IEEE Trans. Inform. Theory*, 20(3):397–399, 1974.

[31] T. Strohmer and R. Heath. Grassmanian frames with applications to coding and communication. *Appl. Comput. Harmon. Anal.*, 14(3):257–275, 2003.

[32] A. Cohen, W. Dahmen, and R. DeVore. Compressed sensing and best k-term approximation. *J. Amer. Math. Soc.*, 22(1):211–231, 2009.

[33] M. Herman and T. Strohmer. High-resolution radar via compressed sensing. *IEEE Trans. Signal Processing*, 57(6):2275–2284, 2009.

[34] J. Laska, P. Boufounos, M. Davenport, and R. Baraniuk. Democracy in action: Quantization, saturation, and compressive sensing. *Preprint*, 2009.

[35] S. Chen, D.L. Donoho, and M.A. Saunders. Atomic decomposition by basis pursuit. *SIAM J. Sci Comp.*, 20(1):33–61, 1999.

[36] I. Esnaola, R.E. Carrillo, J. Garcia-Frias, and K.E. Barner. Orthogonal matching pursuit based recovery for correlated sources with partially disjoint supports. *in Information Sciences and Systems (CISS), 2010 44th Annual Conference on*, pages 1–6, 2010.

[37] D. Donoho, Y. Tsaig, I. Drori, and J-L Starck. Sparse solution of underdetermined linear equations by stagewise orthogonal matching pursuit. *Stanford Technical Report*, pages 1–39, 2006.

[38] Z. Ben-Haim, T. Michaeli, and Y. C. Eldar. Performance bounds and design criteria for estimating finite rate of innovation signals. *Preprint*, 2010.

[39] M. Davenport. Random observations on random observations: Sparse signal acquisition and processing. *PhD thesis, Rice University*, 2010.

[40] J. Treichler, M. Davenport, and R. Baraniuk. Application of compressive sensing to the design of wideband signal acquisition receivers. *In Proc. U.S./Australia Joint Work. Defense Apps. of Signal Processing (DASP)*, 2009.

[41] B. Efron, T. Hastie, I. Johnstone, and R. Tibshirani. Least angle regression. *Annals of Statistics*, 32:407–499, 2004.

[42] I. Daubechies. Time-frequency localization operators: a geometric phase space approach. *Information Theory, IEEE Transactions on*, 34:605–612, 1988.

[43] S. Mallat and Z. Zhang. Matching pursuit in a time-frequency dictionary. *Signal Processing, IEEE Transactions on*, 41:3397–3415, 1993.

[44] S.S. Chen. *Basis Pursuit*. Ph.D. Thesis, Department of Statistics, Stanford University, 1995.

[45] D. Needell and R. Vershynin. Uniform uncertaintity principle and signal reconstruction via regularized orthogonal matching pursuit. *Foundations of Computational Mathematics*, 2008.

[46] I. Esnaola. *Extensions of compressed sensing by exploiting prior knowledge*. Ph.D. Thesis, University of Delaware, 2011.

[47] D. Gabor. A new microscope principle. *Nature*, 161:777–778, 1948.

[48] G.L. Rogers. Experiments in diffraction microscopy. *Proc. Roy. Soc. Edinb.*, 63A:193–221, 1952.

[49] H. El Sum and P. Kirkpatrick. Microscopy by reconstructed wavefronts. *Phys. Rev.*, 85:763, 1952.

[50] E. Leith and J. Upatnieks. Reconstructed wavefronts and communication theory. *J. Opt. Soc. Am.*, 52:1123, 1962.

[51] E. Leith and J. Upatnieks. Wavefront reconstruction with diffused illumination and three dimensional objects. *J. Opt. Soc. Am.*, 54:1295–1301, 1964.

[52] R. Powell and K. Stetson. Interferometric vibration analysis by wavefront reconstruction. *J. Opt. Soc. Am.*, 55:1593, 1965.

[53] K. Stetson and R. Powell. Interferometric hologram evaluation of real time vibration analysis of diffuse objects. *J. Opt. Soc. Am.*, 55:1694–1695, 1965.

[54] M.A. Kronrod, N.S. Merzlyakov, and L.P. Yaroslavsky. Reconstruction of holograms with a computer. *Sov Phys-Tech Phys*, 17:333–334, 1972.

[55] P. Ferraro, D. Alferi, S. De Nicola, L. De Petrocellis, A. Finizio, and G. Pierattini. Quantitative phase-contrast microscopy by a lateral shear approach to digital holographic image reconstruction. *Opt. Lett.*, 31:1405–1407, 2006.

[56] B. Javidi and E. Tajahuerce. Three-dimensional object recognition by use of digital holography. *Opt. Lett.*, 25:610–612, 2000.

[57] M. Paturzo, P. Memmolo, A. Finizio, R. Näsänen, T.J. Naughton, and P. Ferraro. Synthesis and display of dynamic holographic 3d scenes with real-world objects. *Opt. Express*, 18:8806–8815, 2010.

[58] P. Picart and J. Leval. General theoretical formulation of image formation in digital fresnel holography. *J. Opt. Soc. Am. A*, 25(7):1744–1761, 2008.

[59] J.W. Goodman. *Introduction to Fourier Optics, 2nd ed.* McGraw-Hill, 1996.

[60] T. Kreis, M. Adams, and W. Juptner. Methods of digital holography: a comparison. *Proc. SPIE*, 3098:224–233, 1997.

[61] P. Picart, J. Leval, D. Mounier, and S. Gougeon. Some opportunities for vibration analysis with time-averaging in digital fresnel holography. *Appl. Opt.*, 44:337–343, 2005.

[62] P. Ferraro, D. Alferi, S. De Nicola, L. De Petrocellis, A. Finizio, and G. Pierattini. Quantitative phase-contrast microscopy by a lateral shear approach to digital holographic image reconstruction. *Opt. Lett.*, 31:1405–1407, 2006.

[63] P. Memmolo, G. Di Caprio, C. Distante, M. Paturzo, R. Puglisi, D. Balduzzi, A. Galli, G. Coppola, and P. Ferraro. Identification of bovine sperm head for morphometry analysis in quantitative phase-contrast holographic microscopy. *Opt. Express*, 19:23215–23226, 2011.

[64] P. Memmolo, Andrea Finizio, Melania Paturzo, Lisa Miccio, and Pietro Ferraro. Twin-beams digital holography for 3d tracking and quantitative phase-contrast microscopy in microfluidics. *Opt. Express*, 2011.

[65] C. Joo, T. Akkin, B. Cense, B.H. Park, and J.F. de Boer. Spectral-domain optical coherence phase microscopy for quantitative phase-contrast imaging. *Opt. Lett.*, 30:2131–2133, 2005.

[66] E. Cuche, P. Marquet, and C. Depeursinge. Simultaneous amplitude-contrast and quantitative phase-contrast microscopy by numerical reconstruction of fresnel off-axis holograms. *Appl.Opt.*, 38:6994–7001, 1999.

[67] P. Ferraro, S. De Nicola, A. Finizio, G. Coppola, S. Grilli, C. Magro, and G. Pierattini. Compensation of the inherent wave front curvature in digital holographic coherent microscopy for quantitative phase contrast imaging. *Appl. Opt.*, 42(11):1936–1946, 2003.

[68] A. Geltrude, M. Locatelli, R. Meucci, A. Pelagotti, M. Paturzo, P. Poggi, and P. Ferraro. Infrared digital holography for large object investigation. *Digital Holography and Three-Dimensional Imaging, OSA Techinal Digest (CD) (Optical Society of America)*, DWC13, 2011.

[69] N. Pavillon, C. Arfire, I. Bergoend, and C. Depeursinge. Iterative method for zero-order suppression in off-axis digital holography. *Opt. Express*, 18(15):15318–15331, 2010.

[70] T. Kreis. *Digital Recording and Numerical Reconstruction of Wave Fields*. Wiley-VCH Verlag, 2005.

[71] T. Kreis. Frequency analysis of digital holography. *Opt. Eng. (Bellingham)*, 41:771–778, 2002.

[72] T. Kreis. Frequency analysis of digital holography with reconstruction by convolution. *Opt. Eng. (Bellingham)*, 41:1829–1839, 2002.

[73] C.S. Guo, L. Zhang, Z.Y. Rong, and H.T. Wang. Effect of the fill factor of ccd pixels on digital holograms: comment on the paper. *Opt. Eng. (Bellingham)*, 42:2768–2772, 2003.

[74] J. Maylock, B.M. Hennelly, J.B. Mc Donald, Y. Frauel, A. Castro, B. Javidi, and T.J. Naughton. Reduction of speckle in digital holography by discrete fourier filtering. *J. Opt. Soc. Am. A*, 24, 2007.

[75] J. Garcia-Sucerquia, J. A. H. Ramirez, and D. V. Prieto. Reduction of speckle noise in digital holography by using digital image processing. *Optik*, 116:44–48, 2005.

[76] S. Mirza, R. Kumar, and C. Shakher. Study of various preprocessing schemes and wavelet filters for speckle noise reduction in digital speckle pattern interferometric fringes. *Opt. Eng.*, 44(4):045603, 2005.

[77] M. Paturzo, P. Memmolo, L. Miccio, A. Finizio, P. Ferraro, A. Tulino, and B. Javidi. Numerical multiplexing and demultiplexing of digital holographic information for remote reconstruction in amplitude and phase. *Opt. Lett.*, 33(22):2629–2631, 2008.

[78] M. Paturzo, P. Memmolo, A. Tulino, A. Finizio, and P. Ferraro. Investigation of angular multiplexing and de-multiplexing of digital holograms recorded in microscope configuration. *Opt. Express*, 17(11):8709–8718, 2009.

[79] B. Saleh and M. Teich. *Fundamentals of Photonics*. Wiley-Interscience, 1991.

[80] F. Dubois, C. Schockaert, N. Callens, and C. Yourassowsky. Focus plane detection criteria in digital holography microscopy by amplitude analysis. *Opt. Express*, 14(13):5895–5908, 2006.

[81] W. Li, N.C. Loomis, Q. Hu, and C.S. Davis. Focus detection from digital in-line holograms based on spectral l_1 norms. *J. Opt. Soc. Am. A*, 24:3054–3062, 2007.

[82] T.G. Kim and Y.S. Kim. Extraction of a distance parameter in optical scanning holography using axis transformation. *J. Opt. Soc. Korea*, 14:104–108, 2010.

[83] M.L. Tachiki, M. Itoh, and T. Yatagai. Simultaneous depth determination of multiple objects by focus analysis in digital holography. *Appl. Opt.*, 47, 2008.

[84] M. Liebling and M. Unser. Autofocus for digital fresnel holograms by use of a fresnelet-sparsity criterion. *J. Opt. Soc. Am. A*, 21:2424–2430, 2004.

[85] F.C. Groen, I.T. Young, and G. Ligthart. A comparison of different focus functions for use in autofocus algorithms. *Cytometry*, 6:81–91, 1985.

[86] P. Memmolo, C. Distante, M. Paturzo, A. Finizio, P. Ferraro, and B. Javidi. Automatic focusing in digital holography and its application to stretched holograms. *Opt. Lett.*, 36(10):1945–1947, 2011.

[87] H. Tamura, S. Mori, and T. Yamawaki. Textural features corresponding to visual perception. *IEEE Trans. Syst. Man Cyber.*, 8:460–473, 1978.

[88] Y.L. Qi. A relevance feedback retrieval method based on tamura texture. *Second International Symposium on Knowledge Acquisition and Modeling (IEEE, 2009)*, 3:174–177, 2009.

[89] B. Kemper and G. von Bally. Digital holographic microscopy for live cell applications and technical inspection. *Appl. Opt.*, 47(4):A52–A60, 2008.

[90] C. Jackson, R.F. Murphy, and J. Kovacevic. Intelligent acquisition and learning of fluorescence microscope data models. *IEEE Trans. Image Process.*, 18, 2009.

[91] R.A. Hoebe, C.H. Van Oven, T.W.J. Gadella, P.B. Dhonukshe, C.J.F. Van Noorden, and E.M.M. Manders. Controlled light-exposure microscopy reduces photobleaching and phototoxicity in fluorescence live-cell imaging. *Nat. Biotechnol.*, 25:249, 2007.

[92] P Memmolo, M. Paturzo, A. Pelagotti, A. Finizio, P. Ferraro, and B. Javidi. Compression of digital holograms via adaptive sparse representation. *Opt. Lett.*, 35:3883–3885, 2010.

[93] H.M. Smith. *Principles of Holography*. John Wiley and Sons, 1975.

[94] M. Lustig, D. Donoho, and J.M. Pauly. Sparse mri: The application of compressed sensing for rapid mr imaging. *Magn. Reson. Med.*, 58:1182–1195, 2007.

[95] D. Takhar, J. Laska, M. Wakin, M. Duarte, D. Baron, S. Sarvotham, K. Kelly, and R. Baraniuk. A new compressive imaging architecture based on optical-domain compression. *Proc. SPIE*, 6065, 2006.

[96] L. Zhu, Y. Zhu, H Mao, and M. Gu. A new method for sparse signal denoising based on compressed sensing. *Second International Symposium on Knowledge Acquisition and Modeling*, pages 35–38, 2009.

[97] T. Kreis. *Handbook of Holographic Interferometry: Optical and Digital Methods*. Wiley-VCH, 2005.

[98] M.R. Chatterjee and S. Chen. *Digital Holography and Three-Dimensional Display: Principles and Applications, ed. Poon*. T. Springer, 2006.

[99] S. Fukushima, T. Kurokawa, and M. Ohno. Real-time hologram construction and reconstruction using a highresolution spatial light-modulator. *Appl. Phys. Lett.*, 58(8):787–789, 1991.

[100] P. Ferraro, M. Paturzo, P. Memmolo, and A. Finizio. Controlling depth of focus in 3d image reconstructions by flexible and adaptive deformation of digital holograms. *Opt. Lett.*, 34(18):2787–2789, 2009.

[101] S. Boyd and L. Vandenberghe. *Convex Optimization*. Cambridge UP, 2004.